Synaptic plasticity of somatosensory neurons is determined by functional coupling between NMDA receptors and BK channels

Ricardo Gómez[1,2]*, Laura E. Maglio[1,2], Alberto J. Gonzalez-Hernandez[1,2], Belinda Rivero-Perez[1,2], David Bartolomé-Martín[1,2], and Teresa Giraldez[1,2,3]*

Affiliations

[1] Departamento de Ciencias Médicas Básicas-Fisiología, Facultad de Medicina, Universidad de La Laguna, Campus de Ciencias de la Salud s/n 38200, Tenerife, Spain.

[2] Instituto de Tecnologías Biomédicas (ITB), Universidad de La Laguna, Campus de Ciencias de la Salud s/n 38200, Tenerife, Spain.

[3] Lead contact.

* Correspondence: rgomezga@ull.edu.es, giraldez@ull.edu.es

SUMMARY

Postsynaptic N-methyl-D-aspartate receptors (NMDAR) are crucial elements in excitatory synaptic transmission and plasticity due to their role as coincidence detectors of presynaptic and postsynaptic neuronal activity. NMDAR activation is expected to have profound impact in synapse and circuit function, but such activity is not isolated. Here we describe a selective and novel suppression of NMDAR activity by large-conductance Ca^{2+}- and voltage-gated K^+ channels (BK) in basal dendrites of barrel cortex layer 5 pyramidal neurons (BC-L5PN). GluN2A- and GluN2B-containing NMDAR show functional coupling to closely located BK channels, where NMDAR activation provides the Ca^{2+} increase required for BK function. BK-dependent membrane repolarization constitutes a negative feedback mechanism on NMDAR-mediated excitatory stimuli, which distinctively modulates synaptic transmission and long-term plasticity. Accordingly, BC-L5PN exhibiting close NMDAR-BK coupling work as a high-pass filter for incoming afferent inputs, suggesting that BK channels can regulate synaptic input integration to an unexpected extent.

KEYWORDS

N-methyl-D-aspartate receptors (NMDAR), large-conductance Ca^{2+}- and voltage-activated K^+ channels (BK), somatosensory cortex, layer 5 pyramidal neurons (L5PN), synaptic plasticity, spike-timing-dependent plasticity (STDP), long-term synaptic potentiation (LTP)

INTRODUCTION

Glutamate is the primary excitatory chemical transmitter in the mammalian central nervous system (CNS), where glutamatergic signaling is essential for normal functioning of the CNS circuitry, neuronal viability, and behavioral response (Traynelis et al., 2010). Glutamate activates a variety of pre- and postsynaptic receptors, including ionotropic receptors (iGluR) that form ligand-gated cation-permeable ion channels. The iGluR superfamily includes the α-amino-3-hydroxy-5-methyl-4-isoxazolepropionic acid receptors (AMPAR), kainate receptors, and N-methyl-D-aspartate receptors (NMDAR), which are ubiquitously expressed in the CNS (Traynelis et al., 2010).

NMDAR are tetrameric ion channel receptors with high glutamate sensitivity (apparent EC_{50} in the micromolar range) and voltage-dependent block by Mg^{2+} (Mayer et al., 1984; Nowak et al., 1984), slow gating kinetics (Lester et al., 1990), and high permeability to Ca^{2+} (MacDermott et al., 1986; Mayer and Westbrook, 1987) (for a review, see (Paoletti et al., 2013)). These characteristics make postsynaptic NMDAR coincidence detectors of presynaptic and postsynaptic neuronal activity. The presynaptic activity provides the channel with the agonist (glutamate) and the AMPA-driven postsynaptic depolarization causes the removal of the voltage-dependent Mg^{2+} block. The coincidence of these two events leads to NMDAR opening, allowing Ca^{2+} influx through the channel (Caporale and Dan, 2008; Paoletti et al., 2013), which is fundamental in several forms of synaptic plasticity (Malenka and Nicoll, 1993; Markram et al., 1997).

Large-conductance Ca^{2+}- and voltage-gated K^+ (BK) channels are activated by membrane depolarization and relatively high increases in intracellular Ca^{2+} levels (Kshatri et al., 2018a; Latorre et al., 2017). These micromolar Ca^{2+} increases are usually restricted to the immediate vicinity of a Ca^{2+} source, including voltage-gated Ca^{2+} channels (VGCC) (Marrion and Tavalin, 1998) or ryanodine (RyR) (Chavis et al., 1998) and inositol 1,4,5-triphosphate (InsP3R) receptors (Zhao et al., 2010). Additionally, Ca^{2+} influx through other non-selective cation-permeable channels, such as NMDAR, has been shown to activate BK channels in granule cells from the olfactory bulb and dentate gyrus (Isaacson and Murphy, 2001; Zhang et al.,

2018). In these neurons, activation of NMDAR produces the Ca^{2+}-dependent opening of BK channels in somatic and perisomatic areas that, in turn, results in repolarization of the surrounding plasma membrane and the termination of Ca^{2+} entry through NMDAR. In both cases, NMDAR-dependent activation of BK channels has been demonstrated to work as a negative feedback mechanism to modulate neuronal excitability by finishing the NMDAR-mediated excitatory stimulus (Isaacson and Murphy, 2001; Zhang et al., 2018). Therefore, it seems that the same characteristics that make NMDAR a key component in excitatory synaptic transmission and plasticity can paradoxically work as an inhibitory mechanism when NMDAR are located in the proximity of BK channels. However, whether this interaction between NMDAR and BK channels is happening in relevant neuronal locations such as dendrites or dendritic spines, as well as in brain regions other than the above mentioned, has not been elucidated.

Signals derived from the peripheral sensory receptors are transmitted centrally, in turn, to the brainstem, the thalamus, and the neocortex. This incoming sensory information is mainly processed in neuronal microcircuits of the primary somatosensory barrel field area (S1BF), also called “barrel cortex” (BC), and sent onwards to many directly connected downstream cortical and subcortical brain regions (Erzurumlu and Gaspar, 2020; Petersen, 2019). For a long time, layer 4 neurons of the BC were considered the only targets of thalamus afferents. However, several studies demonstrate the direct connection between different thalamic nuclei, such as ventral posterior medial nucleus (VPM), ventrobasal nucleus, or posterior medial nucleus (POm) and layer 5 pyramidal neurons (BC-L5PN) (Agmon and Connors, 1992; Constantinople and Bruno, 2013; El-Boustani et al., 2020; Rodriguez-Moreno et al., 2020). Basal dendrites of BC-L5PN are known to initiate local NMDAR-dependent Ca^{2+} spikes (Nevian et al., 2007; Polsky et al., 2009; Schiller et al., 2000). Coactivation of clustered neighboring basal inputs initiates local dendritic spikes that are mostly mediated by NMDAR and that are characterized by large Ca^{2+} transients restricted to the activated dendritic segments (Polsky et al., 2009; Schiller et al., 2000).

Given the critical role of NMDAR activation in several forms of synaptic plasticity (Malenka and Nicoll, 1993; Markram et al., 1997), in this work we investigated the existence of functional coupling between NMDAR and BK channels in basal dendrites of BC-L5PN and its role in the modulation of synaptic transmission and long-term synaptic plasticity in thalamocortical circuits.

RESULTS

NMDAR activation evokes a BK-mediated outward current in barrel cortex layer 5 pyramidal neurons

Whole-cell voltage-clamp recordings were obtained from mouse BC-L5PN located beneath layer 4 barrels and identified by their large pyramidal-shaped somata (n=108), suggesting that we predominantly recorded from L5a neurons (Figure 1A). Voltage-clamp experiments were performed in Mg^{2+}-free ACSF supplemented with tetrodotoxin (TTX; 1 μM) and glycine (10 μM).

Local application of 200 μM NMDA at basal dendrites of BC-L5PN evoked NMDAR-resembling inward currents in all neurons (Figure 1B). Remarkably, around 40% of the BC-L5PN exhibited an outward current following the inward current at more depolarized membrane potentials (Figure 1B). This outward current exhibited a clear dependence of membrane voltage and its activation occurred at holding potentials positive to -40 mV (Figure 1C). We denominated these two populations of BC-L5PN as “A-type neurons” (lacking the outward current; n=65, 60.2 %) and “B-type neurons” (showing the outward current; n=43, 39.8%). When NMDA application was performed at the same distance from the soma than previously but towards layer 4, inward (but no outward) currents were present in any of the neurons tested (Figure Supp. 1). These results suggest that the NMDA-dependent outward current is restricted to basal dendrites and not evoked at the soma, oblique/truncated dendrites, or the initial segment of the apical dendrite of BC-L5PN.

In the absence of the voltage-dependent blockade produced by Mg^{2+}, NMDAR inward current amplitude (I_{NMDAR}) was directly proportional to the holding potential in both populations (Figure 1D, left panel), indicating that subunit composition of NMDAR responsible for the inward current is similar in both neuronal types. In B-type neurons, the activation of the outward current at more depolarized potentials significantly reduced the total amount of ions flowing through NMDAR (Q_{NMDAR}) (Figure 1D, right panel).

Pharmacological characterization of inward and outward currents was performed in B-type neurons at a holding potential of -20 mV (Figure 1E). The inward current was confirmed to be

driven by NMDAR since it was completely abrogated by selective antagonist D-AP5 (AP5; 100 μM). Moreover, in the presence of AP5, the outward current was also abolished, indicating that NMDAR activation is mandatory to generate the outward current (Figure 1E and 1F). Selective inhibition of GluN2A- and GluN2B-containing NMDAR using 100 nM $ZnCl_2$ and 5 μM ifenprodil, respectively, partially but not fully suppressed outward currents (Figures 1E and 1F). This result suggests that the NMDAR leading to activation of the outward current contains both GluN2A and GluN2B subunits.

The direction of the ionic flow and the clear voltage dependence of the NMDAR-dependent outward currents (Figure 1C) suggest that they may be driven by a voltage-dependent K^+ channel. Additionally, the outward currents found in our study are reminiscent of those previously described in granule cells from olfactory bulb and dentate gyrus after NMDAR activation by local application of glutamate, which were generated by BK channels (Isaacson and Murphy, 2001; Zhang et al., 2018). We tested the role of BK activation in BC-L5PN by applying NMDA in the presence of a specific BK channel pore blocker (1 μM paxilline). As shown in Figures 1E and 1F, paxilline completely abolished the NMDAR-dependent outward current without eliminating the inward component, suggesting that it is generated by BK channels that are activated right after activation of NMDAR.

NMDAR and BK channels are located at functional proximity in B-type BC-L5PN basal dendrites

Our results indicate that NMDAR activation at BC-L5PN basal dendrites provides both the entry of Ca^{2+} and membrane depolarization needed to activate BK channels. To further confirm this hypothesis, we recorded NMDA-evoked currents in the presence of Ca^{2+} chelators that were applied intracellularly through the recording pipette. BAPTA and EGTA have been used to study Ca^{2+} linear diffusion from a Ca^{2+} source (Naraghi and Neher, 1997), constituting useful biochemical tools to estimate the distance between Ca^{2+}-activated K^+ channels and their Ca^{2+} sources (Ngo-Anh et al., 2005). Both chelators present similar affinities for Ca^{2+} but different association rates (BAPTA > EGTA) (Naraghi and Neher, 1997). If both channels are located

in close proximity, BK-dependent outward currents would be recorded in the presence of EGTA, but not in BAPTA. If the distance between both channels is larger, Ca^{2+} flowing through the neighboring Ca^{2+} source would be effectively captured by both chelators before reaching BK, and no outward current would be observed (Naraghi and Neher, 1997). We recapitulated this approach to estimate the distance between NMDAR and BK in BC-L5PN basal dendrites. As shown in Figure 2A, no outward currents were observed in any of the recorded neurons in the presence of the Ca^{2+} chelator BAPTA at concentration 15 mM, confirming the role of Ca^{2+} entering through NMDAR in the activation of BK channels. When the slow chelator EGTA was used at the same concentration, the two populations of BC-L5PN were still distinguishable (Figure 2B). The outward current exhibited a clear dependence of the membrane voltage and its activation occurred at holding potentials positive to -40 mV, as in control conditions, although its amplitude was significantly reduced (Figure 2E vs. Figure 1C). When a lower concentration of BAPTA (1 mM) was used, outward currents were quantitatively identical to those obtained in control conditions (Figure 2F vs. Figure 1C). Altogether, these results suggest that NMDAR and BK channels are located in close proximity in BC-L5PN basal dendrites (estimated range: 15-60 nm; Figure 2G), allowing their specific functional coupling.

GluN2A- and GluN2B-containing NMDAR can functionally couple to activate BK channels

GluN2 subunits determine NMDAR deactivation constants and ion flow (Vicini et al., 1998). We reasoned that the inclusion of different GluN2 subunits in NMDAR would have implications in the efficiency of NMDAR-BK functional coupling. Therefore, we tested if BK would preferentially associate to specific NMDAR subunit combinations.

We first performed proximity ligation assays (PLA) in HEK293T cells co-expressing BK with GluN1/GluN2A or GluN1/GluN2B channels (Figure 3A). Consistent with our pharmacological data (Figure 1F), positive PLA signals were observed in both cases, indicating that NMDAR and BK channels are located in close proximity in the plasma membrane. This association into complexes occurs without any preference between GluN2A and GluN2B subunits (Figure 3B).

To further characterize the functional coupling between NMDAR and BK, we took advantage of the controlled expression of specific channel/subunit combinations in a heterologous expression system, using the inside-out configuration of the patch-clamp technique. This approach allowed us to monitor BK function while controlling intracellular Ca^{2+} concentrations
185 in the bath solution (Giraldez et al., 2005). We included 200 μM NMDA and 10 μM glycine in the recording pipette solution (facing the extracellular side of the membrane patch) to promote NMDAR activation. Figure 3C represents the relative conductance (G) of BK channels at different intracellular Ca^{2+} concentrations (from 0 to 100 μM) from a patch expressing BK channels, without NMDAR. These data correspond to typical Ca^{2+}-dependent activation curves
190 of these channels (Horrigan and Aldrich, 2002; Kshatri et al., 2018b). We reasoned that, in the presence of a Ca^{2+} source such as NMDAR, Ca^{2+} entry towards the intracellular side of the patch should result in a leftward shift of the BK activation curve, which could be compared to those observed at higher Ca^{2+} concentrations in Figure 3C. Consistent with this idea, co-expression of BK channels with GluN1/GluN2A or GluN1/GluN2B NMDAR produced a
195 significant leftward shift of the BK activation curve in zero Ca^{2+} bath solutions (Figure 3D). Interestingly, the magnitude of this shift was comparable to that produced by 10 μM intracellular Ca^{2+} in patches expressing BK alone (Figure 3E and Table Supp. 1). In summary, our results suggest that NMDAR activation increases Ca^{2+} concentration in the vicinity of BK channels, favoring its activation.

200 NMDAR are non-selective cation channels that permeate Na^+, K^+, and Ca^{2+} (Paoletti et al., 2013; Traynelis et al., 2010). Since our inside-out experiments were performed in the absence of Na^+, NMDAR-mediated current influx can only correspond to Ca^{2+} entry. However, under physiological conditions, the proportion of NMDAR current that is carried by Ca^{2+} corresponds to 10-15% of the total current (Burnashev et al., 1995; Garaschuk et al., 1996; Plant et al.,
205 1997). Also, it is known that NMDAR permeability to Ca^{2+} is increased when reducing extracellular Na^+ concentration (Mayer and Westbrook, 1987). Taking this into account, we may be overestimating the effects of NMDAR-dependent Ca^{2+} activation on BK channels in our zero Na^+ experimental conditions. When we recapitulated the inside-out experiments

physiological Na^+ concentrations activation of GluN1/GluN2A or GluN1/GluN2B NMDAR still
210 produced a leftward shift in BK activation (Figures 3G and 3H). Interestingly, GluN1/GluN2B produced larger shifts than GluN1/GluN2A.

Taken together, these results demonstrate that GluN2A- and GluN2B-containing NMDAR can provide the amount of Ca^{2+} required for BK activation, consistent with our data from BC-L5PN basal dendrites (Figure 1F).

215

NMDAR-BK functional coupling is characteristic of one subtype of regular-spiking BC-L5PN

According to their electrophysiological properties, BC neurons are usually classified into fast-spiking nonpyramidal GABAergic interneurons and regular-spiking or intrinsically-bursting
220 pyramidal neurons (Agmon and Connors, 1989, 1992; McCormick et al., 1985). Regular-spiking neurons from layers 5 and 6, where regularly timed trains of action potentials are observed in response to somatic current injection, can be further separated into two different subtypes, characterized by the presence or absence of a depolarizing afterpotential, also referred to as Ca^{2+} spike (Agmon and Connors, 1992; Chagnac-Amitai and Connors, 1989).
225 To address whether the presence of NMDAR-BK functional coupling was restricted to one specific subtype of BC-L5PN whole-cell current-clamp recordings were performed in regular-spiking BC-L5PN (n=197) in the presence of physiological Mg^{2+} and Ca^{2+} concentrations.

The induction of single action potentials in mouse BC-L5PN unveiled the existence of two different populations of neurons, according to the presence (n=130, 66.0%) or absence (n=67,
230 34.0%) of a Ca^{2+} spike (Figure 4B), similar to what was previously described in BC-L5PN from rat and mouse (Agmon and Connors, 1992; Chagnac-Amitai and Connors, 1989; Maglio et al., 2018). We next correlated these two populations of mouse BC-L5PN with the absence or presence of NMDAR-BK complexes in their basal dendrites. After recording the action potential in the current-clamp mode (Figure 4B), we perfused the brain slices with a Mg^{2+}-free solution
235 supplemented with TTX (1 μM) and glycine (10 μM). NMDAR-dependent currents were then recorded in the same neuron, using the voltage-clamp mode, after the application of NMDA at

basal dendrites (Figure 4C). We observed that none of the BC-L5PN exhibiting Ca^{2+} spike presented BK outward currents after NMDAR activation. Conversely, all BC-L5PN in which Ca^{2+} spike was absent showed a robust BK outward current after NMDA application (Figures 4B and 4C). No further differences were found between A-type and B-type neurons regarding their intrinsic properties (Figures 4D to 4G) and evoked action potential characteristics (Figures 4H and 4I), except for those directly related to the presence of the Ca^{2+} spike (Figures 4J and 4K). Therefore, our results show that the presence of NMDAR-BK complexes at basal dendrites is restricted to a population of regular-spiking BC-L5PN characterized by the absence of Ca^{2+} spikes.

BK-dependent inhibition of NMDAR regulates the amplitude of the postsynaptic response

We have demonstrated that BK channels at basal dendrites of BC-L5PN are activated after Ca^{2+} entry through NMDAR that are located in close proximity. In this context, putative NMDAR-BK complexes have an inherent negative feedback loop, whereby NMDAR activation, and the subsequent entry of Ca^{2+}, opens BK channel that allow outward flow of K^+. In turn, this would repolarize the membrane and reinstate the voltage-dependent Mg^{2+} block of NMDAR, truncating the Ca^{2+} entry. Similar interactions have been described for BK channels and VGCC in presynaptic terminals (Griguoli et al., 2016) or NMDAR and small-conductance Ca^{2+}-activated K^+ channels (SK) in postsynaptic terminals of hippocampal CA3-CA1 synapses (Ngo-Anh et al., 2005). If that were the case, the presence of postsynaptic NMDAR-BK complexes in B-type neurons should have a significant impact in synaptic transmission. To address this question, we electrically stimulated the afferent inputs reaching the basal dendrites and recorded the evoked postsynaptic potentials (PSP) in physiological conditions (including Mg^{2+} in the external solution). Presynaptic electrical stimulation of basal afferent inputs was performed in the limit between layers 5 and 6. This approach has been widely described to activate an important contribution of ascending thalamocortical fibers (Manns et al., 2004; Núñez et al., 2012), many of which are known to directly connect with BC-L5PN (Agmon and

265 Connors, 1992; Constantinople and Bruno, 2013; El-Boustani et al., 2020; Rodriguez-Moreno et al., 2020). The presence or absence of a Ca^{2+} spike in the evoked action potential allowed us to classify cells as A-type or B-type BC-L5PN. Electrical stimulation intensity was adjusted to obtain 3-5 mV PSP in all recorded neurons (Figure 5A). Consistent with our proposed mechanism, blocking BK channels with 1 μM paxilline increased NMDAR availability in B-type
270 neurons, thus increasing the PSP amplitude and slowing PSP kinetics (Figure 5B). Further application of AP5 (100 μM) completely abolished the PSP increase and accelerated PSP kinetics (Figure 5B). This result suggests that NMDAR-dependent activation of postsynaptic BK channels is reducing NMDAR contribution to the PSP and therefore regulating synaptic transmission.

275 In basal dendrites of BC-L5PN, coactivation of clustered neighboring basal inputs initiated local dendritic NMDA-dependent spikes that are characterized by large Ca^{2+} transients (Polsky et al., 2009; Schiller et al., 2000). We increased the electrical stimulation intensity applied to the afferent inputs in our experiments to induce these NMDA-dependent Ca^{2+} spikes. We blocked the firing of action potentials by adding the Na^{+} channel blocker QX-314 (2 mM) in the recording
280 pipette. In these experimental conditions, as expected, larger PSP were observed (Figure 5C). Application of paxilline induced an increase in PSP amplitude in B-type neurons, with no effect on A-type neurons (Figures 5C and 5D). Further application of AP5 (100 μM) abolished this increase in B-type neurons and reduced PSP amplitude below control values, to a similar level in both neuron types (Figures 5C and 5D). These results demonstrate that BK channels in
285 NMDAR-BK complexes at B-type neurons basal dendrites can abrogate NMDAR currents even if NMDAR spikes were taking place.

NMDAR-BK complexes at basal dendrites of B-type BC-L5PN increase the threshold for synaptic plasticity induction

290 The existence of an NMDAR-BK negative feedback loop in BC-L5PN basal dendrites, with effects on synaptic transmission, led us to explore their role in other physiological mechanisms

where NMDAR activation and Ca^{2+} entry are mandatory, such as some forms of long-term synaptic plasticity (Malenka and Nicoll, 1993; Markram et al., 1997).

Spike-timing-dependent plasticity (STDP) relays on the coincidence of presynaptic and postsynaptic activity (Bi and Poo, 1998; Markram et al., 1997). The timing and the order of presynaptic and postsynaptic action potentials determine the direction of the change in synaptic strength: a postsynaptic action potential following a presynaptic action potential within a time window of tens of ms results in long-term potentiation (LTP), whereas the reverse order within a similar time window results in long-term depression (LTD) (Bi and Poo, 1998; Feldman, 2000; Markram et al., 1997). Both mechanisms have been demonstrated to be dependent on NMDAR activation (Nevian and Sakmann, 2006). However, only spike-timing-dependent LTP (t-LTP) depends on postsynaptic NMDAR activation and the rise in dendritic spine Ca^{2+} levels ((Nevian and Sakmann, 2006) and Figure Supp. 2). Since we have demonstrated that the NMDAR current is reduced by BK activation in basal dendrites of B-type BC-L5PN, we hypothesized that these neurons should exhibit absent or reduced t-LTP due to the reduction in NMDAR-dependent Ca^{2+} entry. Therefore, we studied the effects of inducing t-LTP by pairing pre- and postsynaptic action potentials in A-type and B-type BC-L5PN. Electrical stimulation of the afferent inputs was used to evoke PSP and pre-post associations were performed at 0.20 Hz (Figure 6A).

A low number of pre-post associations (30 pairings) induced the long-term potentiation of PSP in A-type neurons but produced no effect on B-type neurons (Figure 6B, left panel). This result is consistent with a reduction of the amount of Ca^{2+} entering to basal dendrites through NMDAR, caused by NMDAR-dependent activation of BK channels. The difference between both BC-L5PN populations was abolished when 1 μM paxilline was added in the recording pipette (Figure 6B, right panel), suggesting that BK current inhibition is releasing NMDAR from the BK-induced negative feedback and, thus, favoring the induction of t-LTP. Moreover, the t-LTP extent in both neuron types was significantly greater than in A-type in control conditions (Figure 6B, left vs. right panel), an expected result since BK channels are key regulators of neuronal excitability (Latorre et al., 2017). Interestingly, these data also suggest that BK

channels are present in plasma membrane of both types of BC-L5PN. This was confirmed by recording BK currents in both types of BC-L5PN (Figure Supp. 3).

Since our results suggest that the presence of currents corresponding to NMDAR-BK complexes are restricted to BC-L5PN basal dendrites (Figure 1 vs. Figure Supp. 1), we asked whether the difference in the threshold for synaptic plasticity induction between A-type and B-type neurons was limited to basal dendrites or could also occur in apical dendrites. Electrical stimulation of the appropriate afferent inputs reaching BC-L5PN apical dendrites was used to evoke PSP (Figure 6C) and t-LTP (30 pairings, 0.20 Hz) was induced in both types of neurons. This protocol failed to induce synaptic plasticity in any of the neurons tested (Figure 6D, left panel). When the number of pre-post associations was increased to 90 pairings, t-LTP of a similar extent was induced in both types of neurons, although of significantly lower amplitude than in basal dendrites (Figure 6D, right panel vs. Figure 6B, left panel). These results show no differences between A-type and B-type neurons when the afferent inputs activate apical dendrites, suggesting that functional NMDAR-BK coupling takes place exclusively at basal dendrites of B-type BC-L5PN thus modulating exclusively the long-term synaptic plasticity of neuronal circuits involving these dendrites.

High pre- and postsynaptic coincidence activity relieves BK-dependent NMDAR inhibition

We have demonstrated that BK reduces but does not completely abolish the influx of ions through NMDAR (Figure 1), increasing the threshold for synaptic plasticity induction (Figure 6B). Therefore, it was tempting to hypothesize that by tuning the experimental conditions to force larger NMDAR activation, the amount of Ca^{2+} entering the postsynaptic terminals would eventually reach sufficient levels to induce plasticity in B-type BC-L5PN. In agreement with this idea, we were able to induce t-LTP in B-type neurons by increasing the number of pre-post associations (50 and 90 pairings) (Figure 7A). Modifications in the number of pre-post associations regulate the extent of the t-LTP in BC-L5PN, as previously described in other brain areas such as the hippocampus (Fernández de Sevilla and Buño, 2010; Wittenberg and

Wang, 2006; Zhang et al., 2009). Even so, the extent of potentiation of the PSP recorded from B-type neurons was in all cases significantly reduced compared to that of A-type neurons (Figure 7B). These results demonstrate that the presence of NMDAR-BK complexes at basal dendrites is regulating the threshold to induce synaptic plasticity in B-type BC-L5PN.

The magnitude of t-LTP can be also regulated by increasing the frequency of the pairings or by modifying the time window of the pairings (Caporale and Dan, 2008; Nevian and Sakmann, 2006), although the latter was described to produce a great variability of the STDP output depending on the synapses studied (Caporale and Dan, 2008). We hypothesized that by reducing the time between the pairings (increasing the frequency), a condition could be reached where the BK inhibitory effect on NMDAR completely disappeared. For this purpose, we performed t-LTP experiments (30, 50, and 90 pairings) at a frequency of 0.33 Hz (pre-post pairings delivered every 3 s). As shown in Figure 7C, the t-LTP amplitude in each condition was increased when compared with previous experiments (0.20 Hz) (Figure 7C vs. Figure 7A). Only when 90 pairings were delivered, the extent of PSP potentiation for A-type and B-type neurons was similar (Figure 7D). These results demonstrate that the complete removal of the inhibitory effect of BK on NMDAR can only be achieved in conditions of high pre- and postsynaptic coincidence activity. Moreover, while A-type neurons seemed to reach saturation under a 0.33 Hz STDP protocol, B-type BC-L5PN were still able to discriminate the number of pairings of the protocol.

DISCUSSION

Here we show a novel role of NMDAR and BK functional association in the basal dendrites of a population of regular-spiking BC-L5PN. NMDAR activation and subsequent Ca^{2+} entry
370 promote BK opening, which in turn repolarizes the cell membrane, halting NMDAR activation. Both GluN2A- and GluN2B-containing NMDAR can activate BK channels, although our data suggest that GluN2B-containing NMDAR are more efficient. Functional coupling of NMDAR-BK channels in basal dendrites of this specific BC-L5PN population modulates synaptic transmission and produces an increase in the threshold for synaptic plasticity induction,
375 indicating that NMDAR-BK association critically influences how these neurons distinctively integrate afferent synaptic inputs. In fact, NMDAR-BK functional coupling confers B-type BC-L5PN the ability to work as high-pass filters for incoming inputs depending on the number and frequency of afferent stimuli.

380 Molecular basis of NMDAR-BK functional coupling: Ca^{2+} entry and BK activation

In the CNS, BK channels can be coupled to different Ca^{2+}-conducting channels other than NMDAR, such as VGCC (Marrion and Tavalin, 1998), RyR (Chavis et al., 1998), and InsP3R (Zhao et al., 2010). Such sources provide the Ca^{2+} needed for BK activation, but membrane depolarization is generally provided by a coincident action potential (Griguoli et al., 2016).
385 Interestingly, activation of NMDAR can provide both the membrane depolarization and the Ca^{2+} entry (Paoletti et al., 2013) even in restricted compartments such as the dendritic spine, where the Ca^{2+} concentrations reached after NMDAR activation are in the micromolar range (Higley and Sabatini, 2012; Sabatini et al., 2002). In contrast to previous studies where Mg^{2+}-containing ACSF was used (Isaacson and Murphy, 2001; Zhang et al., 2018), we first
390 characterized the NMDAR-BK functional association in the absence of Mg^{2+}. Our data show that NMDAR-dependent BK activation occurs at potentials positive to -40 mV, within a range of potentials at which the voltage-dependent block by Mg^{2+} is completely released and the NMDAR-dependent current is maximal (Mayer et al., 1984; Nowak et al., 1984). This was

further corroborated in synaptic transmission experiments performed in the presence of Mg^{2+}, where the inhibition of NMDAR by BK channels is evident.

Consistent with previous studies (Isaacson and Murphy, 2001; Zhang et al., 2018), our results demonstrate that the NMDAR-mediated increase in Ca^{2+} concentration in the proximity of BK channels is needed for their activation. The proposed functional coupling mechanism relies on the location of NMDAR and BK channels in close proximity at the plasma membrane. Our results using Ca^{2+} chelators allow us to estimate that these proteins may be situated within a distance range between 15-60 nm from each other. However, this estimation must be taken with caution, since the exact concentration of chelators reached at the dendrites is not known. In fact, our experiments using PLA suggest that the maximum distance between both channels can be even shorter (below 40 nm). Previous work is in favor of a direct association of both channels in the soma, as demonstrated with co-immunoprecipitation biochemical approaches (Zhang et al., 2018). Our results demonstrate strong functional coupling between NMDAR and BK channels in basal dendrites of BC-L5PN, regardless of whether both channels physically interact with each other.

NMDAR-BK functional coupling in long-term synaptic plasticity

Our work provides the first evidence supporting a functional role of NMDAR-BK associations at neuronal dendrites. This result differs from previous studies, where functional coupling between NMDAR and BK channels was suggested to happen at the neuronal soma of granule cells from the olfactory bulb (Isaacson and Murphy, 2001) and the dentate gyrus (Zhang et al., 2018). Also, some evidence points to an existing NMDAR-BK interaction in somata from hippocampal CA1 pyramidal neurons (Zorumski et al., 1989) but not in their dendrites ((Ngo-Anh et al., 2005) and Figure Supp. 4). At the soma, NMDAR-dependent activation of BK channels would mainly constitute a mechanism regulating the action potential shape and controlling neuronal excitability, independently of the inputs reaching from the dendrites.

In dendrites, the presence of NMDAR-BK associations would constitute a negative feedback mechanism that could have dramatic effects on synaptic plasticity mechanisms relying on the

activation of BK-associated NMDAR and Ca^{2+} entry. In the present study, we demonstrate that B-type BC-L5PN, characterized by the presence of NMDAR-BK functional coupling, exhibit a higher threshold for induction of long-term synaptic plasticity. This phenomenon of selective plasticity attenuation is restricted to basal dendrites since the effect was not observed when the afferent inputs for apical dendrites were stimulated. Similar polarity differences (basal vs. apical) affecting synaptic input integration have been described in other brain areas, such as the hippocampus (Cornford et al., 2019).

Interestingly, a recent study points to SK-mediated inhibition of NMDAR as a general mechanism regulating synaptic plasticity in BC-L5PN to BC-L5PN (L5→L5) communication (Jones et al., 2017). Although we cannot fully discard some contribution of this process, we believe that the effects we describe are mainly due to NMDAR-BK functional coupling since NMDAR activation resulted in no outward current other than the BK channel-mediated current. Moreover, the specific inhibition of BK completely abolished the differences between A-type and B-type BC-L5PN after t-LTP induction. Finally, BK-mediated inhibition of NMDAR is preserved when basal afferent inputs are electrically stimulated and is independent of the presence of a back-propagating action potential. Therefore, two different mechanisms inhibiting NMDAR could be present in basal dendrites of BC-L5PN. On the one hand, the SK-mediated mechanism described previously (Jones et al., 2017), which constitutes a backward regulatory mechanism involved in intralayer communication between all types of regular-spiking BC-L5PN and where NMDAR inhibition is dependent of a back-propagating action potential and independent of NMDA activation. On the other hand, our data strongly suggest that NMDAR-BK modulation of synaptic transmission and long-term synaptic plasticity is a forward regulatory mechanism involving thalamocortical projections over a restricted population of BC-L5PN where previous activation of postsynaptic NMDAR is mandatory and the presence of an action potential is no needed.

In this study, we used a STDP protocol to induce long-term potentiation that is delivered at low frequencies. Under these experimental conditions of synaptic stimulation, it has been proposed that GluN1/GluN2B NMDAR make a larger contribution to the total charge transfer than

450 GluN1/GluN2A NMDAR (Erreger et al., 2005), as expected from the slower deactivation rates of GluN2B-containing NMDAR (Vicini et al., 1998). Taking this into account, GluN2B-containing NMDAR should conduct more Ca^{2+} than GluN1/GluN2A channels under our experimental conditions, activating BK more efficiently. That being the case, Ca^{2+} entry through GluN2B-containing NMDAR would be the main contributor to BK activation and thus to the
455 inhibitory mechanism underlying modulation of synaptic transmission and long-term synaptic plasticity. This idea is in agreement with our findings in heterologous expression systems using physiological extracellular Na^{+}, where GluN1/GluN2B NMDAR produced a larger leftward shift in BK activation curve. It also correlates with our observations in basal dendrites of BC-L5PN, where specific blockade of GluN2B-containing NMDAR produced a larger reduction in the
460 NMDA-evoked outward current. In summary, we have demonstrated that both GluN2A- and GluN2B-containing NMDAR are able to activate BK channels both in heterologous expression systems and basal dendrites of BC-L5PN. Whether B-type neurons express a combination of GluN1/GluN2A and GluN1/GluN2B heteromers or GluN1/GluN2A/GluN2B triheteromers (Paoletti et al., 2013) requires further investigation.

465

NMDAR-BK functional coupling in regular-spiking BC-L5PN physiology

An interesting question arises from the fact that NMDAR-BK functional association has been found exclusively in basal dendrites of a subpopulation of regular-spiking BC-L5PN. Is it associated with the specific expression of different GluN2 subunits? This does not seem to be
470 the case, since both neuronal types exhibit similar macroscopic conductances. Although the role of GluN2C and GluN2D subunits was not investigated, a different distribution of these subunits between A-type and B-type neurons would also be reflected in differences in the macroscopic conductance. Therefore, we believe that both populations of BC-L5PN exhibit a similar distribution of GluN2 subunits. Why do NMDAR-BK associations occur selectively in
475 basal dendrites of B-type neurons? Since both cell types express BK channels and NMDAR, a plausible explanation is a mechanism that allows the differential targeting to the dendritic compartment. This could be achieved by engaging specific scaffolding proteins, such as the

receptor for activated C kinase 1 (RACK1) and caveolin-1, which are known to bind both GluN2B NMDAR subunit (Yaka et al., 2002; Yang et al., 2015) and BK channels (Isacson et al., 2007; Wang et al., 2005). In addition, we observed larger BK currents in B-type vs. A-type neurons, suggesting a higher abundance of BK channels in their membrane. Therefore, it is tempting to speculate that the formation of complexes and targeting to basal dendrites of B-type neurons depends on the overall abundance of BK channels available to couple with NMDAR.

Regular-spiking BC-L5PN are classified into two subtypes, according to the presence or absence of a Ca^{2+} spike (Agmon and Connors, 1992; Chagnac-Amitai and Connors, 1989). In this study, we describe two populations of regular-spiking BC-L5PN (≈64% vs. ≈36% for 305 BC-L5PN recorded) distinguished by the absence (A-type) or presence (B-type) of NMDAR-BK functional association in basal dendrites. Interestingly, this distribution highly resembles the electrophysiological characteristics and neuronal ratio previously described in mouse and rat BC-L5PN, based on the presence or absence of a Ca^{2+} spike (Agmon and Connors, 1992; Maglio et al., 2018). Functional NMDAR-BK interaction is exclusively present in basal dendrites from B-type neurons. One of our most relevant findings is that this group of BC-L5PN exhibit a higher threshold for the induction of long-term synaptic potentiation, which is directly related to NMDAR-dependent BK activation in this specific neuronal population. Lacking this molecular brake, A-type neurons reach saturation at a higher frequency, independently of the number of synaptic inputs. This leads us to propose that the BK-dependent inhibition of NMDAR endows B-type neurons with a fine-tuning mechanism to discriminate the amount and frequency of afferent synaptic inputs by selective synaptic plasticity attenuation. As a result of this discrimination capability, we hypothesize that basal dendrites of B-type BC-L5PN are working as a high-pass filter of thalamic afferent inputs, displaying the same output than A-type neurons when a strong stimulus or series of stimuli are reaching the dendrites (e.g., an event of high pre- and postsynaptic coincidence activity) but attenuating the signals below specific cutoff stimuli. The threshold would be mainly determined by the number of BK channels available to functionally couple with NMDAR in basal dendrites of B-type neurons: the larger the number

of BK channels available to form complexes, the higher the threshold to induce synaptic plasticity. This mechanism would provide B-type BC-L5PN with a dynamic range of output responses against the same afferent input stimuli thus increasing the neuronal computational power of somatosensory cortex.

510 Overall, in this study we demonstrate that the presence of NMDAR-BK functional coupling in basal dendrites of a specific set of BC-L5PN modulates the synaptic transmission and synaptic plasticity of thalamocortical circuits, indicating that this association critically influences how these neurons distinctively integrate afferent synaptic inputs.

ACKNOWLEDGMENTS

Authors thank Drs. A. Plested, W. Buño, and A. Pérez-Álvarez for their critical reading of the manuscript. This work has been funded by the European Research Council, under Horizon 2020 Research and Innovation Programme Grant (ERC-CoG-2014 648936) and Spanish Ministerio de Ciencia, Innovación y Universidades (RTI2018-098768-B-I00) to TG. A.J.G.-H. received a Predoctoral Fellowship by Spanish Ministerio de Educación, Cultura y Deporte (FPU15/02528).

AUTHOR CONTRIBUTIONS

Conceptualization, R.G., L.E.M., and T.G.; Methodology, R.G. and L.E.M.; Formal analysis, R.G., L.E.M., A.J.G-H., B.R-P., and D.B-M.; Investigation, R.G., L.E.M., A.J.G-H., B.R-P., and D.B-M.; Writing-Original Draft, R.G. and T.G.; Writing-Review & Editing, R.G. and T.G.; Funding Acquisition, T.G. All authors read, discussed, and approved the manuscript.

DECLARATION OF INTERESTS

The authors declare no competing interests.

530 **FIGURE LEGENDS**

Figure 1. BC-L5PN show NMDAR-dependent outward currents driven by BK channels

(A) Left, general view of a mouse brain slice with the barrel cortex area highlighted in yellow. Right, schematic representation of the experimental design. **(B)** Representative current traces
535 obtained at the indicated holding potentials after NMDA application at basal dendrites. Scale bars represent 10 s and 200 pA. **(C)** Average charge-voltage (Q-V) relationships for A-type (red) and B-type neurons (blue). **(D)** Normalized current-voltage (I-V, left) and Q-V (right) relationships for NMDAR inward currents from A-type and B-type neurons. In **C** and **D**, data points represent mean ± SEM. A-type: n=15, B-type: n=8; *p<0.05 and **p<0.01 (B-type vs. A-
540 type). **(E)** Pharmacological characterization of NMDA-activated currents in BC-L5PN basal dendrites. Normalized charge values for the outward component ($Q_{Outward}$, top) and the inward component (Q_{Inward}, bottom) after the addition of different drugs. Data correspond to mean ± SEM. **p<0.01 and ***p<0.001 (treatment vs. ACSF); #p<0.05, ##p<0.01, and ###p<0.01 (drug+AP5 vs. drug alone). **(F)** Representative current traces obtained at -20 mV after NMDA
545 application at basal dendrites of B-type neurons in control conditions (ACSF, black traces) and after the application of different drugs. Traces are color-coded corresponding to the different treatments shown in panel **E**. Scale bars represent 5 s and 50 pA. In **E** and **F**, AP5, D-AP5 (100 μM; n=6); IFEN, Ifenprodil (5 μM; n=5); PAX, paxilline (1 μM; n=5); Zn^{2+}, $ZnCl_2$ (100 nM; n=5). See also Table Supp. 1.

550

Figure 2. NMDAR and BK channels are located in close proximity in B-type BC-L5PN basal dendrites

(A to C) Representative current traces obtained at the indicated holding potentials after NMDA
555 application at basal dendrites of BC-L5PN in the presence of 15 mM intracellular BAPTA **(A),** 15 mM intracellular EGTA **(B)**, and 1 mM intracellular BAPTA **(C)**. Scale bars represent 10 s and 200 pA. **(D)** Average Q-V relationships corresponding to experiments described in panel

A. Data points represent mean ± SEM; n=18. **(E)** Average Q-V relationships corresponding to experiments in panel **B**. Data points represent mean ± SEM. A-type: n=8, B-type: n=5. **(F)** Average Q-V relationships corresponding to experiments in panel **C**. Data points represent mean ± SEM. A-type: n=9, B-type: n=5. Dashed lines represent data for A-type and B-type neurons in the absence of Ca^{2+} chelators (same data from Figure 1C). In **E** and **F**, *p<0.05 and **p<0.01 (B-type vs. A-type). **(G)** Schematic representation of the relative location of NMDAR and BK in the plasma membrane. The distances are estimated from the experimental data. See also Table Supp. 1.

Figure 3. BK channels are functionally coupled to GluN2A- and GluN2B-containing NMDAR

(A) Representative confocal microscopy images of PLA experiments in HEK293 cells expressing the protein combinations indicated at the top of the images. Each row corresponds to an imaging channel (top, DAPI, blue; middle, NMDAR, green; bottom, PLA, red). **(B)** Average PLA signals/μm^2 for all conditions shown in panel **A**. Data points represent individual measurements and each condition was studied in four independent experiments. Black lines represent mean ± SEM. ***p<0.001 vs. untransfected cells (UNTRANSF), BK alone (BK), and GluN1 alone (GluN1) conditions. **(C)** Normalized conductance-voltage (G-V) relationships obtained from patches expressing BK channels alone (n=12), in the presence of different intracellular Ca^{2+} concentrations in symmetrical K^+ solutions. Data points represent mean ± SEM. Lines represent the best fit of a Boltzmann equation to the data. Ca^{2+} concentrations are color-coded as indicated in the graph legend. **(D)** Normalized G-V relationships from patches co-expressing BK channels with GluN1/GluN2A (left; n=6) or GluN1/GluN2B (right; n=5) in the absence of intracellular Ca^{2+}. Data points represent mean ± SEM. Lines represent the best fit of a Boltzmann equation to the data. **(E)** The graph represents V_{half} values obtained from experiments depicted in panels **C** and **D**. Data points represent individual experiment measurements and lines represent mean ± SEM. **(F)** Representative current traces in physiological brain slices solutions recorded from HEK293 cells expressing BK alone (top),

BK+GluN1/GluN2A (middle), and BK+GluN1/GluN2B (bottom). Scale bars represent 30 ms and 2000 pA. **(G)** Normalized G-V relationships for BK channels coexpressed with GluN1/GluN2A (left, red; n=6) or GluN1/GluN2B (right, blue; n=5) in the absence of intracellular Ca^{2+}. Black traces in both graphs correspond to G-V curves of the BK channels expressed alone (n=11). Data points represent mean ± SEM. Lines represent the best fit of a Boltzmann equation to the data. **(H)** Summary of V_{half} values from experiments in panel G. Data points represent individual experiment measurements and lines represent mean ± SEM. ***p<0.001 vs. BK alone. See also Table Supp. 1.

Figure 4. NMDAR-BK functional coupling is restricted to a subpopulation of regular spiking BC-L5PN

(A) Representative current traces elicited with 500-ms depolarizing steps from -100 to 320 pA obtained from A-type (red) and B-type (blue) BC-L5PN. Scale bars represent 200 ms and 50 mV. **(B)** Single action potentials recorded from the same neurons shown in panel **A**. The arrow points to the Ca^{2+} spike characteristic of A-type BC-L5PN. Scale bars represent 100 ms and 20 mV. **(C)** NMDA-evoked currents at -20 and -60 mV holding potentials recorded from the same neurons depicted in panels **A** and **B** using the voltage-clamp configuration with a Mg^{2+}-free external solution containing 1 μM TTX and 10 μM glycine. Scale bars represent 5 s and 150 pA. **(D to K)** Resting membrane potential **(D)**, input resistance **(E)**, cell capacitance **(F)**, action potential frequency **(G)**, threshold **(H)**, amplitude **(I)**, and duration **(J)**, and afterhyperpolarization amplitude **(K)** values. Data correspond to individual (symbols) and median and 25th-75th percentile (boxes) values from A-type (red, n=130) and B-type (blue, n=67) BC-L5PN, except for panel **G**, where data points represent mean ± SEM. In **J** and **K**, ***p<0.001 (B-type vs. A-type). See also Figure Supp. 5 and Table Supp. 1.

Figure 5. BK channels reduce NMDAR contribution to synaptically-evoked postsynaptic potentials

(A) Representative synaptically-evoked postsynaptic potential (PSP) traces recorded from A-type (top, red) and B-type (bottom, blue) neurons in control conditions (ACSF, left) and after
615 the application of 1 μM paxilline (PAX, middle) or 1 μM PAX plus 100 μM AP5 (PAX+AP5, right). Scale bars represent 50 ms and 3 mV. **(B)** Representation of the normalized PSP amplitude (top left), rise time (bottom left), PSP area (top right), rise time (bottom left), and decay time (bottom right) values under the experimental conditions in panel **A**. Data points represent individual experiment measurements (n=7 in both types of neurons) and boxes
620 represent median and 25th-75th percentile values. **(C)** Representative synaptically-evoked PSP traces recorded from A-type (top, red) and B-type (bottom, blue) neurons after increasing the electrical stimulation intensity applied to the afferent inputs. Similar conditions as in panel **A** (ACSF, PAX, PAX+AP5) were studied. The pipette solution included 2 mM QX-314 to avoid action potential firing. Scale bars represent 50 ms and 3 mV. **(D)** Representation of the PSP
625 amplitude (top left), area (top right), rise time (bottom left), and decay time (bottom right) values corresponding to the experimental conditions shown in panel **C**. Data points represent individual experiment measurements and boxes represent median and 25th-75th percentile values. A-type: n=5; B-type: n=6. In **B** and **D**, *p<0.05, **p<0.01, and ***p<0.001. See also Table Supp. 1.

630

Figure 6. NMDAR-BK functional coupling determines the threshold for t-LTP induction

(A) Schematic representation of the experimental design used to induce synaptic long-term potentiation through basal afferent synaptic inputs in BC-L5PN. **(B)** STDP-induced long-term potentiation (t-LTP) development over time in A-type (red) and B-type (blue) neurons in control
635 conditions (ACSF, left) and in the presence of 500 nM intracellular paxilline (PAX, right). Data points represent mean ± SEM. A-type (ACSF): n=6; B-type (ACSF): n=4; A-type (PAX): n=6; B-type (PAX): n=4. ***p<0.001 (t-LTP vs. basal conditions). **(C)** Schematic representation of the experimental design used to induce synaptic long-term potentiation through apical afferent synaptic inputs in BC-L5PN. **(D)** t-LTP development over time in A-type (red) and B-type (blue)
640 neurons in control conditions (ACSF) using a 30 (left) or 90 (right) pairing STDP protocol. Data

points represent mean ± SEM. A-type (30 pairings): n=3; A-type (90 pairings): n=6; and B-type (90 pairings): n=3. See also Figure Supp. 2, Figure Supp. 3, and Table Supp. 1.

Figure 7. High pre- and postsynaptic coincidence activity relieves BK-dependent NMDAR inhibition

(A) Time course of t-LTP development over time in A-type (red) and B-type (blue) neurons using a 30 (left), 50 (middle), or 90 (right) pairings STDP protocol following the experimental design represented in Figure 6A. Data points represent mean ± SEM. A-type (30 pairings): n=6, B-type (30 pairings): n=4; A-type (50 pairings): n=6; B-type (50 pairings): n=4; A-type (90 pairings): n=6; B-type (90 pairings): n=5. Data in the left panel (30 pairings) are the same as in Figure 6B. **(B)** Summary of t-LTP extent for A-type (red) and B-type (blue) neurons under the experimental conditions depicted in panel **A** (0.20 Hz). **(C)** Time course of t-LTP development over time in A-type (red) and B-type (blue) neurons using a 30 (left), 50 (middle), or 90 (right) pairing STDP protocol at a frequency of 0.33 Hz. Data points represent mean ± SEM. A-type (30 pairings): n=6, B-type (30 pairings): n=4; A-type (50 pairings): n=7; B-type (50 pairings): n=5; A-type (90 pairings): n=5; B-type (90 pairings): n=6. **(D)** Summary of t-LTP extent for A-type (red) and B-type (blue) neurons under the experimental conditions depicted in panel **C** (0.33 Hz). In **A** and **C**, ***$p<0.001$ (t-LTP vs. basal conditions). In **B** and **D**, ###$p<0.001$ (B-type vs. A-type). See also Table Supp. 1.

660 **MATERIAL and METHODS**

KEY RESOURCES TABLE

REAGENT or RESOURCE	SOURCE	IDENTIFIER
Antibodies		
Rabbit polyclonal anti-Maxi potassium channel α (BK α subunit)	Abcam	Cat#ab219072
Goat polyclonal anti-NMDAR1 (GluN1 subunit)	Novus Biologicals	Cat#NB100-41105
Mouse monoclonal anti-NMDAε1 (GluN2A subunit)	Santa Cruz Biotechnology	Cat#sc-515148
Mouse monoclonal anti-NMDAε2 (GluN2B subunit)	Santa Cruz Biotechnology	Cat#sc-365597
Chemicals, Peptides, and Recombinant Proteins		
D-AP5 (D-2-amino-5-phosphonovalerate, AP5)	Tocris	Cat#0106
BAPTA (1,2-bis(o-aminophenoxy)ethane-N,N,N',N'-tetraacetic acid)	Abcam	Cat#ab144924
EGTA (Ethylene glycol-bis(β-aminoethyl ether)-N,N,N',N'-tetraacetic acid)	Sigma-Aldrich	Cat#E4378
Glycine	Tocris	Cat#0219
HEDTA (N-(2-Hydroxyethyl)ethylenediamine-N,N',N'-triacetic acid)	Sigma-Aldrich	Cat#H8126
Ifenprodil	Tocris	Cat#0545
NMDA (N-methyl-D-aspartate)	Tocris	Cat#0114
Paxilline	Tocris	Cat#2006
QX-314 (N-(2,6-Dimethylphenylcarbamoylmethyl)-triethylammonium bromide)	Tocris	Cat#1014
TTX (Tetrodotoxin)	Tocris	Cat#1078
$ZnCl_2$ (Zinc chloride)	Merck	Cat#1.08816.1000
Critical Commercial Assays		
PLA: DuoLink In Situ Detection Reagents Red	Sigma-Aldrich	Cat#DUO92008
PLA: DuoLink In Situ PLA Probe Anti-Rabbit PLUS Antibody	Sigma-Aldrich	Cat#DUO92002; RRID:AB_10950581
PLA: DuoLink In Situ PLA Probe Anti-Mouse MINUS Antibody	Sigma-Aldrich	Cat#DUO92004; RRID:AB_2713942
PLA: DuoLink In Situ PLA Probe Anti-Goat MINUS Antibody	Sigma-Aldrich	Cat#DUO92006; RRID:AB_10953178
Cell transfection: jetPRIME reagent	Polyplus transfection	Cat#114-75
Experimental Models: Cell Lines		
Human: HEK293T cells	ATCC	Cat#CRL-3216
Experimental Models: Organisms/Strains		
Mouse: C57BL/6J	The Jackson Laboratory	Cat#000664; RRID:IMSR_JAX:000664
Recombinant DNA		
Plasmid: pBNJ-hsloTAG	(Giraldez et al., 2005)	N/A
Plasmid: pEYFP-NR1a	(Luo et al., 2002)	RRID: Addgene_17928
Plasmid: pEGFP-NR2A	(Luo et al., 2002)	RRID: Addgene_17924
Plasmid: pEGFP-NR2B	(Luo et al., 2002)	RRID: Addgene_17925
Software and Algorithms		

pClamp software package (Clampex, Clampfit)	Molecular Devices	https://www.moleculardevices.com/products/axon-patch-clamp-system/acquisition-and-analysis-software/pclamp-software-suite RRID:SCR_011323
MaxChelator	(Bers et al., 2010)	https://somapp.ucdmc.ucdavis.edu/pharmacology/bers/maxchelator/index.html
Prism8	GraphPad Inc.	https://www.graphpad.com/scientific-software/prism/ RRID:SCR_002798
Fiji	(Schindelin et al., 2012)	http://fiji.sc RRID:SCR_002285

LEAD CONTACT AND MATERIALS AVAILABILITY

Further information and requests for reagents and resources should be directed to the lead contact author, Teresa Giraldez (giraldez@ull.edu.es).

EXPERIMENTAL MODEL

All the procedures for handling and sacrificing animals followed the Spanish (Real Decreto 53/2013) and European Commission (Directive 2010/63/EU) guidelines for the care and use of laboratory animals and were approved by the Ethics Committee (CEIBA) of the Universidad de La Laguna. C57BL/6J mice (The Jackson Laboratory #000664) were housed in standard laboratory cages with *ad libitum* access to water and food in temperature- and humidity-controlled rooms under a 12:12 h light-dark cycle at the Universidad de La Laguna animal facilities (registry number ES380230024514).

METHOD DETAILS

Acute mice brain slices

C57BL/6J adult male mice (postnatal 28-36) were slightly anesthetized with isoflurane, decapitated, and the brain quickly removed and immersed in an ice-cold high-sucrose "cutting solution" (composition in mM: 189 sucrose, 10 glucose, 26 $NaHCO_3$, 3 KCl, 5 $MgSO_4$, 0.1 $CaCl_2$, and 1.25 NaH_2PO_4), continuously bubbled with carbogen (95% oxygen/5% carbon
685 dioxide). Coronal brain slices of 350 µm of thickness were obtained using a Microm HM650V vibratome (Thermo Scientific). These slices were maintained during 1-1.5 h in artificial cerebrospinal fluid (ACSF; composition in mM: 124 NaCl, 2.69 KCl, 1.25 KH_2PO_4, 2 $MgSO_4$, 26 $NaHCO_3$, 10 glucose, 2 $CaCl_2$, and 0.4 ascorbic acid; pH 7.35) bubbled with carbogen at room temperature (22-24ºC) for recovery. After recovery, brain slices were transferred to a
690 recording chamber mounted onto an upright Olympus BX51WI microscope (Olympus) equipped with 10x/40x water immersion objectives, where they were continuously perfused with carbogen-bubbled ACSF.

Electrophysiology in brain slices

695 Electrophysiological recordings in brain slices were performed using the whole-cell configuration of the patch-clamp technique (Hamill et al., 1981). Patch pipettes were made from 1.50 OD/0.86 ID borosilicate glass capillaries (GC150F-10; Harvard Apparatus) using a P-97 micropipette puller (Sutter Instruments) and had resistances of 5-8 MΩ when filled with the internal solution (composition in mM: 135 $KMeSO_4$, 10 KCl, 10 HEPES, 5 NaCl, 2.5 ATP-
700 Mg, and 0.3 GTP-Na; pH 7.3). Recordings were obtained with a MultiClamp 700A amplifier (Molecular Devices). Series resistance was compensated (≈70%) and recordings were rejected when the access resistance varied >20% during the experiment. Data were acquired at 10 kHz and lowpass-filtered at 4 kHz. Signals were fed to a Pentium-based PC through an Axon Digidata 1550B interface board (Molecular Devices). The pClamp software (Molecular
705 Devices) was used for stimulus generation, data display, acquisition, storage, and analysis. All experiments were performed at room temperature (22-24ºC).

Pyramidal neurons from layer 5 of the somatosensory 1 barrel field area (S1BF, namely "barrel cortex") were visualized by infrared microscopy and differential interference contrast (IR-DIC)

using an ORCA-Flash4.0LT digital camera (Hamamatsu). Barrel cortex layer 5 pyramidal
710 neurons (BC-L5PN) were identified by their location (just below layer 4), shape (characteristic somatic morphology), and electrophysiological properties (only regular-spiking neurons were used in the study; intrinsically-bursting and fast-spiking neurons were discarded), suggesting that we predominantly recorded from slender-tufted neurons located in layer 5a, as described previously (Manns et al., 2004; Núñez et al., 2012).

715 ***Recording of N-methyl-D-aspartate-evoked currents***

N-methyl-D-aspartate (NMDA; 200 μM) was locally delivered ("puff" application) at different dendritic locations of BC-L5PN through a glass pipette using a PMI-100 Pressure MicroInjector (Dagan Corporation) at 1 bar during 50-200 ms (Figure 1A and Figure Supp. 1A). Puff pipettes were made from GC150F-10 borosilicate glass capillaries as patch pipettes. Responses
720 evoked by NMDA application at different holding potentials (from -60 to 0 mV) were recorded from BC-L5PN using the voltage-clamp mode in the whole-cell configuration of the patch-clamp technique in a Mg^{2+}-free ACSF, where an equimolar substitution of Mg^{2+} with Ca^{2+} was made to maintain total extracellular divalent cation concentration. The Mg^{2+}-free ACSF was supplemented with tetrodotoxin (TTX; 1 μM) to avoid neuronal action potential-dependent
725 communication and with the NMDAR coagonist glycine (10 μM) to ensure NMDAR activation. The duration of the NMDA puff application was adjusted to obtain inward currents of 200-250 pA of peak amplitude at -60 mV. NMDA local application was performed at different BC-L5PN locations: basal dendrites (Figure 1), oblique dendrites/initial segment of the apical dendrite (Figure Supp. 1), and apical dendrites (not shown). We were unable to record NMDA-evoked
730 currents when NMDA was applied at apical dendrites of BC-L5PN under our experimental conditions, which may suggest that we predominantly recorded from slender-tufted neurons. In some experiments, responses evoked by NMDA application at different holding potentials (from -70 to -10 mV) were recorded from hippocampal CA1 pyramidal neurons using the same experimental conditions described above (Figure Supp. 4).

735 NMDA-evoked inward currents (I_{Inward}, namely I_{NMDAR}) were measured as the maximum peak amplitude, whereas NMDA-evoked inward and outward total ionic charges (Q_{Inward} and $Q_{Outward}$,

respectively; namely Q_{NMDAR} and Q_{BK}) were calculated as the area under the recorded trace and the zero current level. The I_{NMDAR}, Q_{NMDAR}, and $Q_{Outward}/Q_{Inward}$ ratio were calculated and represented as a function of the holding potential (Figures 1C and 1D). BC-L5PN were classified according to the absence (A-type neurons) or presence (B-type neurons) of an NMDA-evoked outward current.

Pharmacological characterization of inward and outward currents was performed in B-type neurons at a holding potential of -20 mV (Figures 1E and 1F). All drugs were added to the bath solution. In some experiments, BAPTA (15 or 1 mM) and EGTA (15 mM) Ca^{2+} chelators were added to the recording pipette (Figure 2), where an equimolar substitution of $KMeSO_4$ with BAPTA-K or EGTA-K was made to maintain the total internal K^+ concentration.

Action potential and postsynaptic potential recordings

BC-L5PN were recorded using the current-clamp mode in the whole-cell configuration of the patch-clamp technique in normal ACSF (2 $MgSO_4$ and 2 $CaCl_2$). Patch pipettes and internal solution were the same as described previously for voltage-clamp recordings.

Current-voltage (I-V) relationships were elicited with 500-ms depolarizing steps from -100 to 320 pA (Figure 4A). Resting membrane potential, action potential firing, and cell input resistance were calculated from these recordings (Figure 4D to 4G).

Action potentials were obtained either by presynaptic electrical stimulation of basal afferent inputs or by a brief current injection through the recording pipette (5 ms, 200-400 pA) since no differences between both methods were found (see Figure Supp. 5A for a comparison). Action potential characteristics were calculated from these recordings as depicted in Figures Supp. 5C and 5D. According to the absence or presence of a Ca^{2+} spike following the action potential, two different populations of BC-L5PN were distinguished, as previously described (Agmon and Connors, 1992; Chagnac-Amitai and Connors, 1989; Maglio et al., 2018). These populations inversely correlated with those described after NMDA-evoked current recordings, that is, A-type neurons exhibited Ca^{2+} spikes but no NMDAR-evoked outward currents, whereas B-type neurons exhibited NMDAR-evoked outward currents but no Ca^{2+} spikes (Figure 4B and 4C).

Postsynaptic potentials (PSP) were obtained by presynaptic electrical stimulation of basal
765 afferent inputs in the limit between layers 5 and 6 since it is widely described that it activates an important contribution of ascending thalamocortical fibers (Manns et al., 2004; Núñez et al., 2012), many of which are known to directly connect with BC-L5PN (Agmon and Connors, 1992; Constantinople and Bruno, 2013; El-Boustani et al., 2020; Rodriguez-Moreno et al., 2020). Stimulation pipettes were made from 1.50 OD/1.02 ID thick septum theta borosilicate glass
770 capillaries (TST150-6; World Precision Instruments) using a P-97 micropipette puller and filled with ACSF. Single pulses (100 μs) were delivered at 0.20 Hz by a Master-8 pulse Stimulator (A.M.P.I.) through an ISU-165 isolation unit (Cibertec). Stimulus intensity was adjusted to obtain 3-5 mV PSP responses and was unchanged for the entire experiment (Figure 5A). In some experiments (Figure 5C), stimulus intensity was adjusted to evoke NMDAR-dependent
775 Ca^{2+} spikes. In these experiments, the voltage-gated Na^{+} channel blocker QX-314 (2 mM) was included in the recording pipette to avoid the possibility of generating action potentials, as described (Núñez et al., 2012; Polsky et al., 2009).

In all experiments, basal PSP were recorded for 10-15 min before any drug application. BK blocker paxilline (1 μM) and NMDAR antagonist AP5 (100 μM) were applied in the bath. The
780 parameters studied were PSP peak amplitude, area, and rise and decay times (Figures 5B and 5D).

Spike-timing-dependent plasticity

Induction of spike-timing-dependent plasticity (STDP) long-term potentiation (t-LTP) was achieved by pairing pre- and postsynaptic action potentials 10 ms away. Presynaptic action
785 potentials were evoked by electrical stimulation of basal afferent inputs as described above and are recorded as PSP responses (Figure 6A). Postsynaptic action potentials were elicited by a brief current injection through the recording pipette (5 ms, 200-400 pA) as aforementioned. Basal PSP were recorded for 10-15 min before the pre-post associations were induced (30, 50, and 90 pairings were studied). After that, PSP were recorded for another 50-60 min.
790 Amplitude of PSP 5 min before (-5 to 0 min interval) and 50 min after (45 to 50 min interval) the t-LTP induction protocol were measured to compare the extent of the PSP potentiation.

For a pharmacological characterization of the t-LTP, BK blocker paxilline (500 nM) was applied intracellularly (through the recording pipette) (Figure 6B, right panel), whereas the NMDAR antagonist AP5 (100 μM) was applied in the bath (Figure Supp. 2B).

795 In some experiments, presynaptic stimulation of apical afferent inputs was paired with evoked postsynaptic action potentials to compare basal vs. apical t-LTP in BC-L5PN (Figure 6D). In these experiments, presynaptic electrical stimulation was performed in the limit between layers 1 and 2 (Figure 6C).

BK current recordings

800 BK currents from BC-L5PN were recorded as the paxilline-sensitive currents using the voltage-clamp mode in the whole-cell configuration of the patch-clamp technique in normal ACSF (2 $MgSO_4$ and 2 $CaCl_2$) supplemented with TTX (1 μM). Patch pipettes were filled with a modified recording solution (composition in mM: 123 $KMeSO_3$, 9 NaCl, 9 HEPES, 0.9 EGTA, 14 Tris-phosphocreatine, 2 ATP-Mg, 2 ATP-Na, and 0.3 GTP-Tris; pH 7.3), as previously described

805 (Whitt et al., 2018). I-V relationships were elicited from a holding potential of -70 mV, stepping from -110 to 90 mV for 150 ms in 20 mV increments (Figure Supp. 3). BK currents were isolated by current subtraction after bath application of the BK blocker paxilline (1 μM) and normalized to BC-L5PN capacitance (Whitt et al., 2018).

810 **HEK293T cell line culture and transient ion channel transfection**

Human embryonic kidney (HEK293T; ATCC #CRL-3216) cells were grown on 12-mm poly-lysine treated glass coverslips in Dulbecco's Modified Eagle Medium supplemented with 10% fetal bovine serum and 1% penicillin-streptomycin. Cells were maintained in an incubator at 37ºC in a 5% carbon dioxide atmosphere. Transient transfection of different combinations of

815 cDNA plasmids encoding for BK alpha subunit (pBNJ-hsloTAG) and GluN1 (pEYFP-NR1a), GluN2A (pEGFP-NR2A), and GluN2B (pEGFP-NR2B) NMDAR subunits was performed using jetPRIME reagent (Polyplus Transfection). pBNJ-hsloTAG plasmid was generated in the lab (Giraldez et al., 2005) and pEYFP-NR1a (Addgene plasmid #17928), pEGFP-NR2A (Addgene

plasmid #17924), and pEGFP-NR2B (Addgene plasmid #17925) plasmids were a gift from
820 Stefano Vicini (Luo et al., 2002).

Electrophysiology in HEK293T cells

Poly-lysine treated glass coverslips containing the HEK293T cells expressing different combinations of NMDAR and BK channels were placed in a recording chamber mounted onto
825 an inverted Nikon Eclipse Ti-U microscope (Nikon) equipped with 20x/40x objectives. Electrophysiological recordings were carried out 36–48 h post-transfection using the inside-out configuration of the patch-clamp technique (Figure 3C to 3H) (Hamill et al., 1981; Kshatri et al., 2018b). All experiments were performed at room temperature (22-24ºC).

Inside-out BK current recordings in symmetrical K^+ solutions

830 Patch pipettes were fabricated from GC150F-10 borosilicate glass capillaries as aforementioned and then fire-polished with a MF-200 microforge (World Precision Instruments) to obtain a tip resistance of 2–5 MΩ when filled with the recording solution (composition in mM: 80 $KMeSO_3$, 60 N-methylglucamine-$MeSO_3$, 20 HEPES, 2 KCl, and 2 $CaCl_2$; pH 7.4). Recording solution was supplemented with NMDA (200 μM) and glycine (10 μM) to ensure
835 NMDAR activation during the experiment, as previously described (Borschel et al., 2011; Xiong et al., 1998). Cells were superfused with a bath solution, containing (in mM): 80 $KMeSO_3$, 60 N-methylglucamine-$MeSO_3$, 20 HEPES, 2 KCl, and 1 HEDTA (pH 7.4). $CaCl_2$ was added to obtain the desired free Ca^{2+} concentration. For Ca^{2+} solutions containing 100 μM Ca^{2+}, no HEDTA chelator was added. The total amount of $CaCl_2$ needed to obtain the desired Ca^{2+}
840 concentration was calculated using the MaxChelator program (MAXC; (Bers et al., 2010)) and free Ca^{2+} was confirmed using a Ca^{2+}-sensitive electrode (ThermoLab Systems). Stimulus generation and data acquisition were controlled and analyzed with the pClamp software package. The currents were amplified using an Axopatch-200B amplifier and digitized using a Digidata 1550A interface board (Molecular Devices). Subsequently, the data were acquired at
845 100 kHz and lowpass-filtered at 5 kHz. BK currents were elicited from a holding potential of -

60 mV, stepping from -100 to 200 mV for 25 ms in 20 mV increments and then repolarizing to -80 mV for 100 ms to record the "tail currents".

Conductance-voltage (G-V) curves were generated from tail current amplitudes normalized to the maximum amplitude obtained in 100 μM Ca^{2+}. A Boltzmann equation was fitted to the data according to the following equation:

$$G / G_{max} = 1 / (1 + \exp((V_m - V_{half}) / z))$$

where V_{half} is the voltage of half-maximum activation, z is the slope of the curve, V_m is the test potential, and G_{max} is the maximal conductance (Figures 3C and 3D).

Inside-out BK current recordings in slices recording solutions

In some experiments (Figures 3F to 3H), inside-out recordings were performed using slightly modified brain slices solutions (see below). Briefly, the recording solution contained normal ACSF supplemented with NMDA (200 μM) and glycine (10 μM) to ensure NMDAR activation during the experiment. The bath solution contained (in mM): 135 $KMeSO_4$, 10 KCl, 10 HEPES, 5 NaCl, 2.5 ATP-Mg, and 0.3 GTP-Na (pH 7.3), and was supplemented with EGTA (10 mM) to obtain a Ca^{2+}-free solution. BK currents were elicited from a holding potential of -60 mV, stepping from -100 to 200 mV for 100 ms in 20 mV increments.

G-V curves were generated from I-V relationships, calculating the relative G for each test potential according to the following equation:

$$G = I / (V_m - E_{rev})$$

where I is the current amplitude at the end of the depolarizing pulse for each test potential (V_m) and E_{rev} is the reversal potential for K^+ with the solutions used. Individual G values were then normalized to maximal conductance (G_{max}) and plotted as a function of V_m to obtain the G-V curves. A Boltzmann equation was fitted to the resultant values, as described before, and the V_{half} were obtained.

Proximity Ligation Assay

Proximity ligation assay (PLA) was performed using a commercially available kit (DuoLink; Sigma-Aldrich). HEK293T cells expressing different combinations of NMDAR and BK channels

were fixed with 4% paraformaldehyde for 20 min, permeabilized, and then blocked for 1 h at 37ºC to avoid non-specific binding of antibodies. BK channel was detected using a rabbit polyclonal anti-Maxi K^+ channel alpha subunit primary antibody (1:200, #ab219072; Abcam). GluN1, GluN2A, and GluN2B subunits of NMDAR were detected using a goat polyclonal anti-NMDAR1 (1:200, #NB100-41105; Novus Biologicals) and mouse monoclonal anti-NMDAε1 (1:200, #sc-515148; Santa Cruz Biotechnology) and anti-NMDAε2 (1:200, #sc-365597; Santa Cruz Biotechnology) primary antibodies, respectively. Secondary antibodies conjugated with oligonucleotides were supplied with the PLA DuoLink kit. Controls consisted of untransfected HEK293T cells or cells where only the BK alpha subunit or any of the NMDAR subunits alone were expressed (e.g., GluN1, as shown in Figure 3A). Image acquisition was performed using a Leica TS8 inverted confocal microscope (Leica Biosystems) and analysis and quantification were performed using Duolink Image Tool software (Sigma-Aldrich). Additional analysis and representation were performed using Fiji (Schindelin et al., 2012). A fluorescent dot corresponded with one protein-protein interaction, that is, where the proteins of interest are close enough (less than 40 nm) to be detected by the PLA technique (Alam, 2018). Results are expressed as the number of fluorescent dots (PLA signals) per cell area (in μm^2). Four independent experiments were performed for each condition.

Drugs and Reagents

D-AP5 (D-2-amino-5-phosphonovalerate, AP5), glycine, ifenprodil (IFEN), N-methyl-D-aspartate (NMDA), paxilline (PAX), QX-314, and tetrodotoxin (TTX) were purchased from Tocris. EGTA and HEDTA were purchased from Sigma-Aldrich. BAPTA and $ZnCl_2$ were purchased from Abcam and Merck, respectively. See Key Resources Table for complete references of all the drugs used in this study. Drugs were dissolved in the adequate solvent (DMSO or water) and prepared as 1000-10000x stock solutions of the desired final concentration. Subsequent dilution in ACSF (bath application) or pipette recording solution was performed to obtain the final concentration used in the experiments.

Statistical analysis

Data were analyzed with GraphPad Prism8 (GraphPad). Data are shown as mean ± SEM or as individual values (symbols) plus median and 25th-75th percentile (boxes) values. A two-tailed
905 t-test was used to analyze data from the same neuron measured twice (before/after) (e.g., pharmacological characterization in Figure 1E or t-LTP in Figures 6 and 7). A two-tailed unpaired t-test (Gaussian distribution) or a Mann-Whitney U test (non-Gaussian distribution) were used to analyze A-type vs. B-type BC-L5PN electrophysiological data. Kruskal-Wallis test was used to analyze PLA data. Statistical significance is stated as *$p<0.05$, **$p<0.01$, or
910 ***$p<0.001$. Statistical details related to main and supplementary figures are specified in Table Supp. 1.

REFERENCES

915 Agmon, A., and Connors, B.W. (1989). Repetitive burst-firing neurons in the deep layers of mouse somatosensory cortex. Neurosci Lett *99*, 137-141.

Agmon, A., and Connors, B.W. (1992). Correlation between intrinsic firing patterns and thalamocortical synaptic responses of neurons in mouse barrel cortex. J Neurosci *12*, 319-329.

Alam, M.S. (2018). Proximity Ligation Assay (PLA). Curr Protoc Immunol *123*, e58.

920 Bers, D.M., Patton, C.W., and Nuccitelli, R. (2010). A practical guide to the preparation of Ca(2+) buffers. Methods Cell Biol *99*, 1-26.

Bi, G.Q., and Poo, M.M. (1998). Synaptic modifications in cultured hippocampal neurons: dependence on spike timing, synaptic strength, and postsynaptic cell type. J Neurosci *18*, 10464-10472.

Borschel, W.F., Murthy, S.E., Kasperek, E.M., and Popescu, G.K. (2011). NMDA receptor activation

925 requires remodelling of intersubunit contacts within ligand-binding heterodimers. Nat Commun *2*, 498.

Burnashev, N., Zhou, Z., Neher, E., and Sakmann, B. (1995). Fractional calcium currents through recombinant GluR channels of the NMDA, AMPA and kainate receptor subtypes. J Physiol *485 (Pt 2)*, 403-418.

930 Caporale, N., and Dan, Y. (2008). Spike timing-dependent plasticity: a Hebbian learning rule. Annu Rev Neurosci *31*, 25-46.

Chagnac-Amitai, Y., and Connors, B.W. (1989). Synchronized excitation and inhibition driven by intrinsically bursting neurons in neocortex. J Neurophysiol *62*, 1149-1162.

Chavis, P., Ango, F., Michel, J.M., Bockaert, J., and Fagni, L. (1998). Modulation of big K+ channel activity

935 by ryanodine receptors and L-type Ca2+ channels in neurons. Eur J Neurosci *10*, 2322-2327.

Constantinople, C.M., and Bruno, R.M. (2013). Deep cortical layers are activated directly by thalamus. Science *340*, 1591-1594.

Cornford, J.H., Mercier, M.S., Leite, M., Magloire, V., Hausser, M., and Kullmann, D.M. (2019). Dendritic NMDA receptors in parvalbumin neurons enable strong and stable neuronal assemblies. Elife *8*.

940 El-Boustani, S., Sermet, B.S., Foustoukos, G., Oram, T.B., Yizhar, O., and Petersen, C.C.H. (2020). Anatomically and functionally distinct thalamocortical inputs to primary and secondary mouse whisker somatosensory cortices. Nat Commun *11*, 3342.

Erreger, K., Dravid, S.M., Banke, T.G., Wyllie, D.J., and Traynelis, S.F. (2005). Subunit-specific gating controls rat NR1/NR2A and NR1/NR2B NMDA channel kinetics and synaptic signalling profiles. J
945 Physiol *563*, 345-358.

Erzurumlu, R.S., and Gaspar, P. (2020). How the Barrel Cortex Became a Working Model for Developmental Plasticity: A Historical Perspective. J Neurosci *40*, 6460-6473.

Feldman, D.E. (2000). Timing-based LTP and LTD at vertical inputs to layer II/III pyramidal cells in rat barrel cortex. Neuron *27*, 45-56.

950 Fernández de Sevilla, D., and Buño, W. (2010). The muscarinic long-term enhancement of NMDA and AMPA receptor-mediated transmission at Schaffer collateral synapses develop through different intracellular mechanisms. J Neurosci *30*, 11032-11042.

Garaschuk, O., Schneggenburger, R., Schirra, C., Tempia, F., and Konnerth, A. (1996). Fractional Ca2+ currents through somatic and dendritic glutamate receptor channels of rat hippocampal CA1
955 pyramidal neurones. J Physiol *491 (Pt 3)*, 757-772.

Giraldez, T., Hughes, T.E., and Sigworth, F.J. (2005). Generation of functional fluorescent BK channels by random insertion of GFP variants. J Gen Physiol *126*, 429-438.

Griguoli, M., Sgritta, M., and Cherubini, E. (2016). Presynaptic BK channels control transmitter release: physiological relevance and potential therapeutic implications. J Physiol *594*, 3489-3500.

960 Hamill, O.P., Marty, A., Neher, E., Sakmann, B., and Sigworth, F.J. (1981). Improved patch-clamp techniques for high-resolution current recording from cells and cell-free membrane patches. Pflugers Arch *391*, 85-100.

Higley, M.J., and Sabatini, B.L. (2012). Calcium signaling in dendritic spines. Cold Spring Harb Perspect Biol *4*, a005686.

965 Horrigan, F.T., and Aldrich, R.W. (2002). Coupling between voltage sensor activation, Ca2+ binding and channel opening in large conductance (BK) potassium channels. J Gen Physiol *120*, 267-305.

Isaacson, J.S., and Murphy, G.J. (2001). Glutamate-mediated extrasynaptic inhibition: direct coupling of NMDA receptors to Ca(2+)-activated K+ channels. Neuron *31*, 1027-1034.

Isacson, C.K., Lu, Q., Karas, R.H., and Cox, D.H. (2007). RACK1 is a BKCa channel binding protein. Am J
970 Physiol *292*, C1459-1466.

Jones, S.L., To, M.S., and Stuart, G.J. (2017). Dendritic small conductance calcium-activated potassium channels activated by action potentials suppress EPSPs and gate spike-timing dependent synaptic plasticity. Elife *6*.

Kshatri, A.S., Gonzalez-Hernandez, A., and Giraldez, T. (2018a). Physiological Roles and Therapeutic
975 Potential of Ca(2+) Activated Potassium Channels in the Nervous System. Front Mol Neurosci *11*, 258.

Kshatri, A.S., Gonzalez-Hernandez, A.J., and Giraldez, T. (2018b). Functional validation of Ca(2+)-binding residues from the crystal structure of the BK ion channel. Biochim Biophys Acta Biomembr *1860*, 943-952.

980 Latorre, R., Castillo, K., Carrasquel-Ursulaez, W., Sepulveda, R.V., Gonzalez-Nilo, F., Gonzalez, C., and Alvarez, O. (2017). Molecular Determinants of BK Channel Functional Diversity and Functioning. Physiol Rev *97*, 39-87.

Lester, R.A., Clements, J.D., Westbrook, G.L., and Jahr, C.E. (1990). Channel kinetics determine the time course of NMDA receptor-mediated synaptic currents. Nature *346*, 565-567.

985 Luo, J.H., Fu, Z.Y., Losi, G., Kim, B.G., Prybylowski, K., Vissel, B., and Vicini, S. (2002). Functional expression of distinct NMDA channel subunits tagged with green fluorescent protein in hippocampal neurons in culture. Neuropharmacology *42*, 306-318.

MacDermott, A.B., Mayer, M.L., Westbrook, G.L., Smith, S.J., and Barker, J.L. (1986). NMDA-receptor activation increases cytoplasmic calcium concentration in cultured spinal cord neurones. Nature
990 *321*, 519-522.

Maglio, L.E., Noriega-Prieto, J.A., Maraver, M.J., and Fernández de Sevilla, D. (2018). Endocannabinoid-Dependent Long-Term Potentiation of Synaptic Transmission at Rat Barrel Cortex. Cereb Cortex *28*, 1568-1581.

Malenka, R.C., and Nicoll, R.A. (1993). NMDA-receptor-dependent synaptic plasticity: multiple forms and mechanisms. Trends Neurosci *16*, 521-527.

Manns, I.D., Sakmann, B., and Brecht, M. (2004). Sub- and suprathreshold receptive field properties of pyramidal neurones in layers 5A and 5B of rat somatosensory barrel cortex. J Physiol *556*, 601-622.

Markram, H., Lubke, J., Frotscher, M., and Sakmann, B. (1997). Regulation of synaptic efficacy by coincidence of postsynaptic APs and EPSPs. Science *275*, 213-215.

Marrion, N.V., and Tavalin, S.J. (1998). Selective activation of Ca2+-activated K+ channels by co-localized Ca2+ channels in hippocampal neurons. Nature *395*, 900-905.

Mayer, M.L., and Westbrook, G.L. (1987). Permeation and block of N-methyl-D-aspartic acid receptor channels by divalent cations in mouse cultured central neurones. J Physiol *394*, 501-527.

Mayer, M.L., Westbrook, G.L., and Guthrie, P.B. (1984). Voltage-dependent block by Mg2+ of NMDA responses in spinal cord neurones. Nature *309*, 261-263.

McCormick, D.A., Connors, B.W., Lighthall, J.W., and Prince, D.A. (1985). Comparative electrophysiology of pyramidal and sparsely spiny stellate neurons of the neocortex. J Neurophysiol *54*, 782-806.

Naraghi, M., and Neher, E. (1997). Linearized buffered Ca2+ diffusion in microdomains and its implications for calculation of [Ca2+] at the mouth of a calcium channel. J Neurosci *17*, 6961-6973.

Nevian, T., Larkum, M.E., Polsky, A., and Schiller, J. (2007). Properties of basal dendrites of layer 5 pyramidal neurons: a direct patch-clamp recording study. Nat Neurosci *10*, 206-214.

Nevian, T., and Sakmann, B. (2006). Spine Ca2+ signaling in spike-timing-dependent plasticity. J Neurosci *26*, 11001-11013.

1015 Ngo-Anh, T.J., Bloodgood, B.L., Lin, M., Sabatini, B.L., Maylie, J., and Adelman, J.P. (2005). SK channels and NMDA receptors form a Ca2+-mediated feedback loop in dendritic spines. Nat Neurosci *8*, 642-649.

Nowak, L., Bregestovski, P., Ascher, P., Herbet, A., and Prochiantz, A. (1984). Magnesium gates glutamate-activated channels in mouse central neurones. Nature *307*, 462-465.

1020 Núñez, A., Domínguez, S., Buño, W., and Fernández de Sevilla, D. (2012). Cholinergic-mediated response enhancement in barrel cortex layer V pyramidal neurons. J Neurophysiol *108*, 1656-1668.

Paoletti, P., Bellone, C., and Zhou, Q. (2013). NMDA receptor subunit diversity: impact on receptor properties, synaptic plasticity and disease. Nat Rev Neurosci *14*, 383-400.

Petersen, C.C.H. (2019). Sensorimotor processing in the rodent barrel cortex. Nat Rev Neurosci *20*,
1025 533-546.

Plant, T., Schirra, C., Garaschuk, O., Rossier, J., and Konnerth, A. (1997). Molecular determinants of NMDA receptor function in GABAergic neurones of rat forebrain. J Physiol *499 (Pt 1)*, 47-63.

Polsky, A., Mel, B., and Schiller, J. (2009). Encoding and decoding bursts by NMDA spikes in basal dendrites of layer 5 pyramidal neurons. J Neurosci *29*, 11891-11903.

1030 Rodriguez-Moreno, J., Porrero, C., Rollenhagen, A., Rubio-Teves, M., Casas-Torremocha, D., Alonso-Nanclares, L., Yakoubi, R., Santuy, A., Merchan-Perez, A., DeFelipe, J.*, et al.* (2020). Area-Specific Synapse Structure in Branched Posterior Nucleus Axons Reveals a New Level of Complexity in Thalamocortical Networks. J Neurosci *40*, 2663-2679.

Sabatini, B.L., Oertner, T.G., and Svoboda, K. (2002). The life cycle of Ca(2+) ions in dendritic spines.
1035 Neuron *33*, 439-452.

Schiller, J., Major, G., Koester, H.J., and Schiller, Y. (2000). NMDA spikes in basal dendrites of cortical pyramidal neurons. Nature *404*, 285-289.

Schindelin, J., Arganda-Carreras, I., Frise, E., Kaynig, V., Longair, M., Pietzsch, T., Preibisch, S., Rueden, C., Saalfeld, S., Schmid, B.*, et al.* (2012). Fiji: an open-source platform for biological-image analysis.
1040 Nat Methods *9*, 676-682.

Traynelis, S.F., Wollmuth, L.P., McBain, C.J., Menniti, F.S., Vance, K.M., Ogden, K.K., Hansen, K.B., Yuan, H., Myers, S.J., and Dingledine, R. (2010). Glutamate receptor ion channels: structure, regulation, and function. Pharmacol Rev *62*, 405-496.

Vicini, S., Wang, J.F., Li, J.H., Zhu, W.J., Wang, Y.H., Luo, J.H., Wolfe, B.B., and Grayson, D.R. (1998). Functional and pharmacological differences between recombinant N-methyl-D-aspartate receptors. J Neurophysiol *79*, 555-566.

Wang, X.L., Ye, D., Peterson, T.E., Cao, S., Shah, V.H., Katusic, Z.S., Sieck, G.C., and Lee, H.C. (2005). Caveolae targeting and regulation of large conductance Ca(2+)-activated K+ channels in vascular endothelial cells. J Biol Chem *280*, 11656-11664.

Whitt, J.P., McNally, B.A., and Meredith, A.L. (2018). Differential contribution of Ca(2+) sources to day and night BK current activation in the circadian clock. J Gen Physiol *150*, 259-275.

Wittenberg, G.M., and Wang, S.S. (2006). Malleability of spike-timing-dependent plasticity at the CA3-CA1 synapse. J Neurosci *26*, 6610-6617.

Xiong, Z.G., Raouf, R., Lu, W.Y., Wang, L.Y., Orser, B.A., Dudek, E.M., Browning, M.D., and MacDonald, J.F. (1998). Regulation of N-methyl-D-aspartate receptor function by constitutively active protein kinase C. Mol Pharmacol *54*, 1055-1063.

Yaka, R., Thornton, C., Vagts, A.J., Phamluong, K., Bonci, A., and Ron, D. (2002). NMDA receptor function is regulated by the inhibitory scaffolding protein, RACK1. Proc Natl Acad Sci U.S.A. *99*, 5710-5715.

Yang, J.X., Hua, L., Li, Y.Q., Jiang, Y.Y., Han, D., Liu, H., Tang, Q.Q., Yang, X.N., Yin, C., Hao, L.Y.*, et al.* (2015). Caveolin-1 in the anterior cingulate cortex modulates chronic neuropathic pain via regulation of NMDA receptor 2B subunit. J Neurosci *35*, 36-52.

Zhang, J., Guan, X., Li, Q., Meredith, A.L., Pan, H.L., and Yan, J. (2018). Glutamate-activated BK channel complexes formed with NMDA receptors. Proc Natl Acad Sci U.S.A. *115*, E9006-E9014.

Zhang, J.C., Lau, P.M., and Bi, G.Q. (2009). Gain in sensitivity and loss in temporal contrast of STDP by dopaminergic modulation at hippocampal synapses. Proc Natl Acad Sci U.S.A. *106*, 13028-13033.

Zhao, G., Neeb, Z.P., Leo, M.D., Pachuau, J., Adebiyi, A., Ouyang, K., Chen, J., and Jaggar, J.H. (2010). Type 1 IP3 receptors activate BKCa channels via local molecular coupling in arterial smooth muscle cells. J Gen Physiol *136*, 283-291.

1070 Zorumski, C.F., Thio, L.L., Clark, G.D., and Clifford, D.B. (1989). Calcium influx through N-methyl-D-aspartate channels activates a potassium current in postnatal rat hippocampal neurons. Neurosci Lett *99*, 293-299.

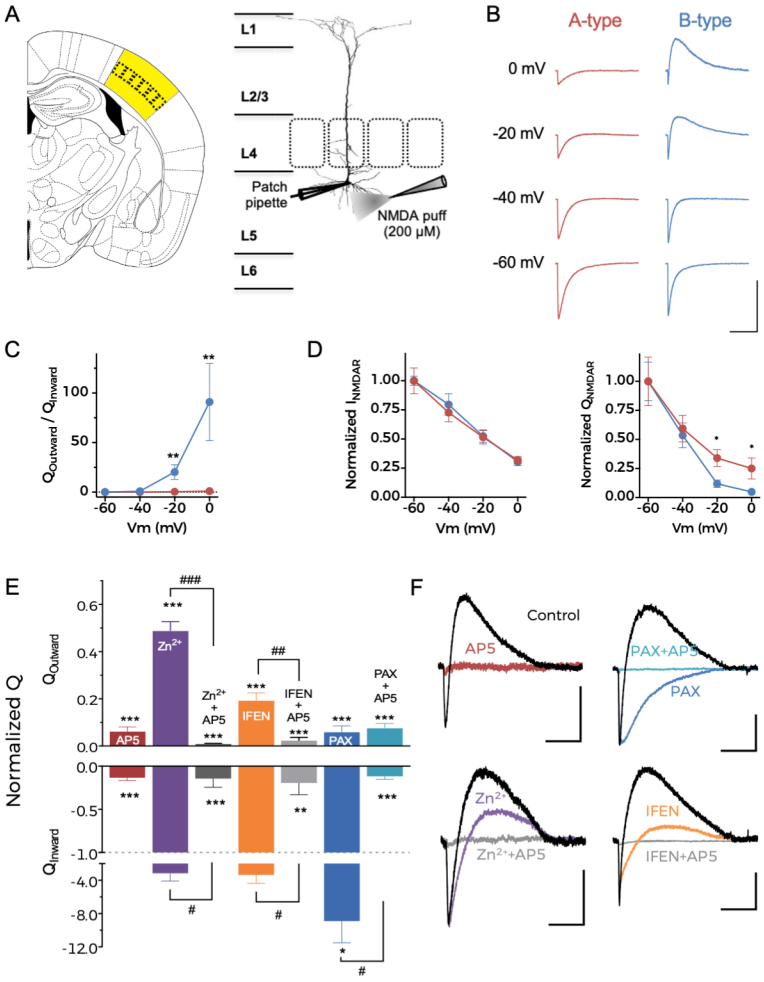

Figure 1 Gómez et al

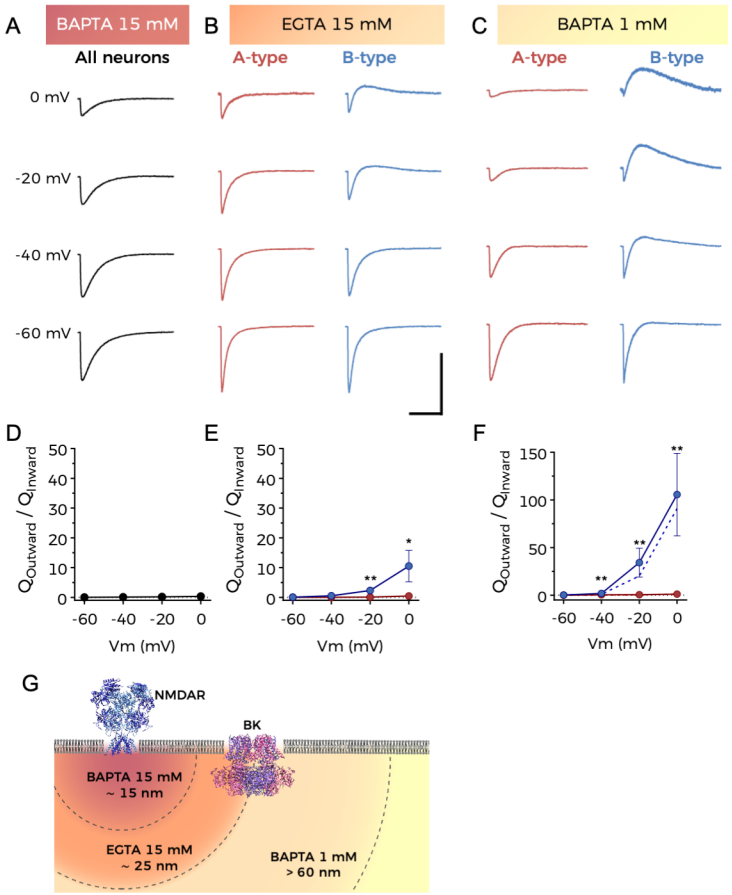

Figure 2 Gómez et al

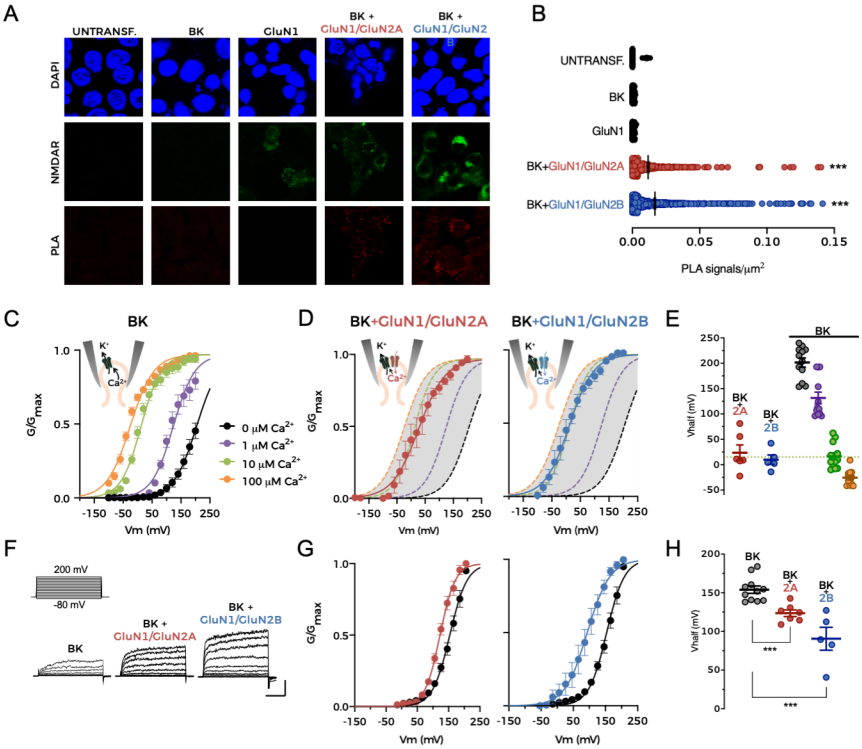

Figure 3 Gómez et al

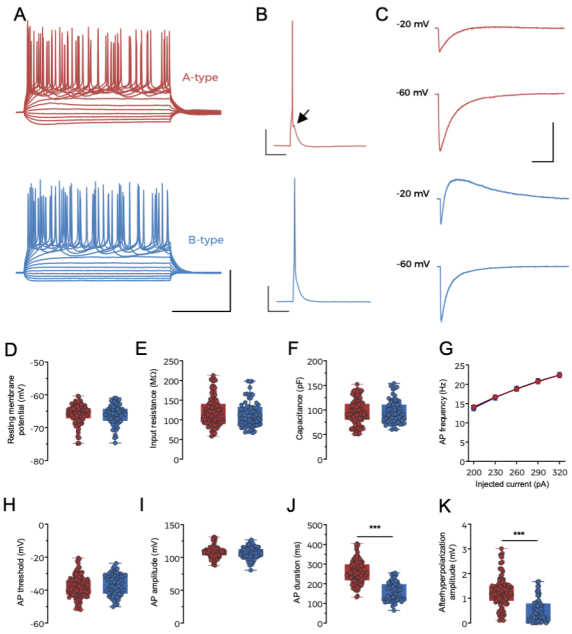

Figure 4 Gómez et al

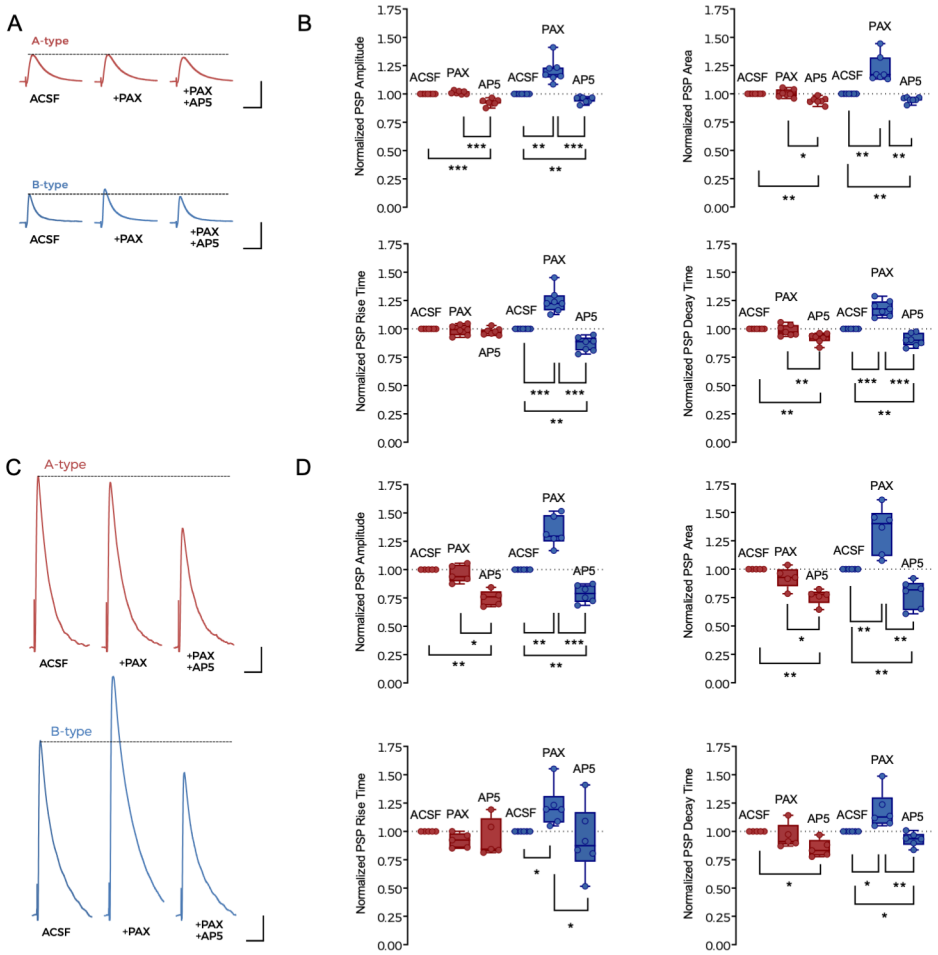

Figure 5 Gómez et al

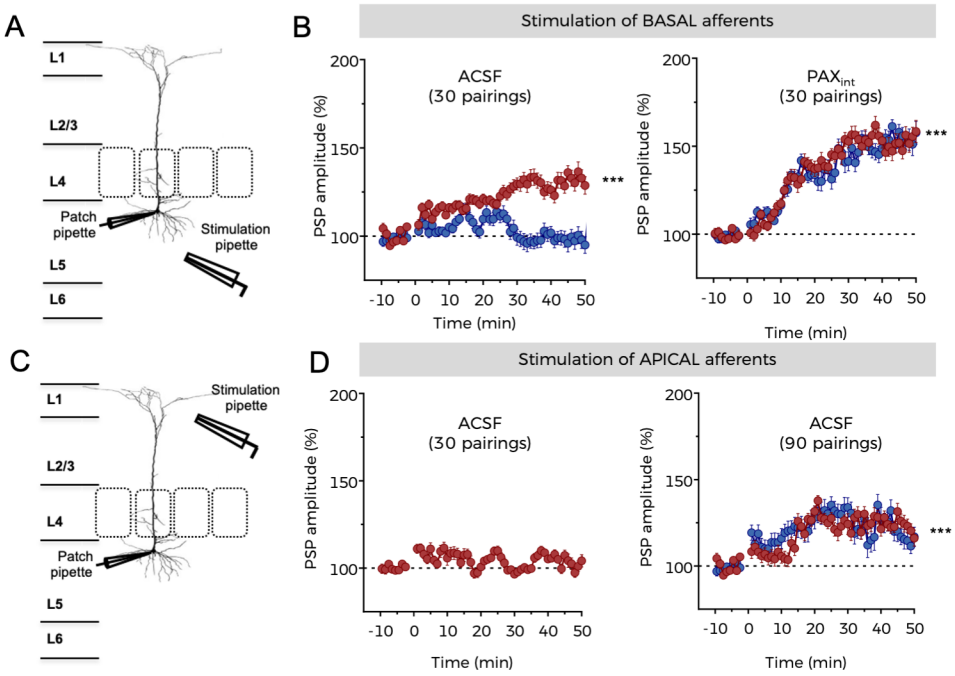

Figure 6 Gómez et al

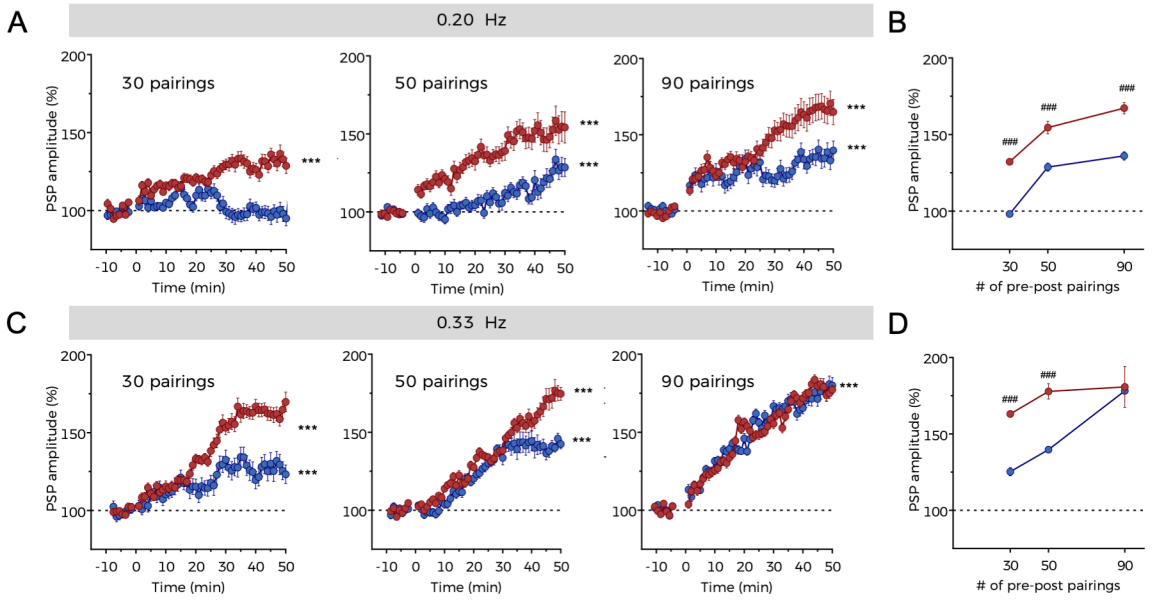

Figure 7 Gómez et al